COLORADO
Department of Transportation

CDOT Office of Applied Research

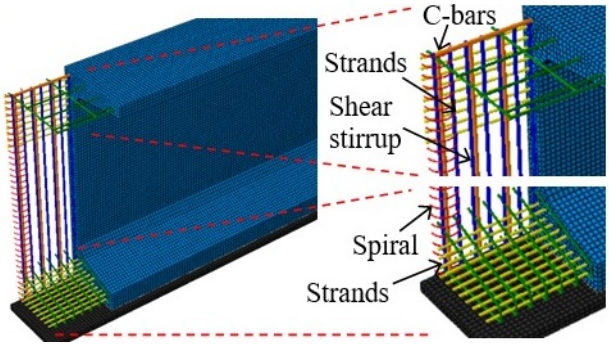

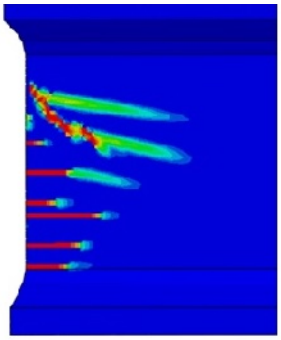

Mitigation of End Zone Cracking in Prestressed Concrete Girders

Yail Jimmy Kim

December 2024
CDOT-2024-12

Technical Report Documentation Page

1. Report No.	2. Government Accession No.	3. Recipient's Catalog No.
CDOT-2024-12		

4. Title and Subtitle	5. Report Date
Mitigation of End Zone Cracking in Prestressed Concrete Girders	12/31/2024
	6. Performing Organization Code

7. Author(s)	8. Performing Organization Report No.
Yail Jimmy Kim	

9. Performing Organization Name and Address	10. Work Unit No. (TRAIS)
University of Colorado Denver 1200 Larimer St., Denver, CO 80217	11. Contract or Grant No.

12. Sponsoring Agency Name and Address	13. Type of Report and Period Covered
Colorado Department of Transportation Office of Applied Research 2829 W. Howard Place Denver, CO 80204	14. Sponsoring Agency Code

15. Supplementary Notes

Prepared in cooperation with the US Department of Transportation, Federal Highway Administration

16. Abstract

This report presents two major aspects related to the end-zone behavior of prestressed concrete bulb-tee girders: i) laboratory experiments and ii) full-scale finite element modeling. The first part of the report discusses the behavior of anchorage zones, also known as end zones, with discrete rebars and continuous meshes. To examine the implications of various reinforcing schemes on the capacity, cracking, and failure of end zones, 50 block specimens are loaded and their responses are analyzed. While concrete splitting originates from local tension generated near the axial compression, the location of cracking is dominated by the path of stress trajectories related to the number of rebars, which is not recognized in the case of the meshed specimens. A two-stage analytical model is formulated to predict the magnitude of bursting forces and figure out the effects of several parameters on the response of the end zones. The applicability of existing design expressions is assessed and the need for follow-up research is delineated. The second part of the report deals with the effectiveness of various reinforcing schemes in the end zones of prestressed concrete bulb-tee girders. The default girder taken from the Colorado Department of Transportation includes C-bars and spirals, which are intended to control cracking, and three-dimensional finite element analysis is conducted. The formulated models are used to evaluate the breadth of end zones, strain responses, cracking patterns, damage amounts, and splitting forces, depending upon the configuration of the end-zone reinforcement. Whereas the short-term crack width of the girder may not be an immediate concern, its long-term width is found to surpass the established limit of 0.007 in. In this regard, multiple C-bars should be placed to address concerns about undesirable cracking.

Implementation

The research has found that using multiple C-bars is beneficial for controlling end-zone cracks in both the short and long term. Provided that rebar congestion is not a concern during the fabrication of steel cages, two to three No. 6 or No. 7 C-bars spaced 6 in. apart are recommended along with welded wire fabric (W4×W4).

17. Keywords	18. Distribution Statement
bridges; cracking; end zones; girders; prestressed concrete	This document is available on CDOT's website: https://www.codot.gov/programs/research

19. Security Classif. (of this report)	20. Security Classif. (of this page)	21. No. of Pages	22. Price
Unclassified	Unclassified		

The contents of this report reflect the views of the author(s), who is(are) responsible for the facts and accuracy of the data presented herein. The contents do not necessarily reflect the official views of the Colorado Department of Transportation or the Federal Highway Administration. This report does not constitute a standard, specification, or regulation.

Acknowledgments

The research team would like to acknowledge valuable guidance and thought-provoking comments provided by Andrew Pott, Mike Bean, Jacob O'Brien, and Michael Collins (Staff Bridge, CDOT) as well as Spencer Tucker (FHWA). The research team is also grateful to Thien Tran (Applied Research and Innovation Branch, CDOT) for his comprehensive support and administrative assistance.

Executive Summary

This report presents two major aspects related to the end-zone behavior of prestressed concrete bulb-tee girders: i) laboratory experiments and ii) full-scale finite element modeling. The first part of the report discusses the behavior of anchorage zones, also known as end zones, with discrete rebars and continuous meshes. To examine the implications of various reinforcing schemes on the capacity, cracking, and failure of end zones, 50 block specimens are loaded and their responses are analyzed. Test parameters include the types of rebar materials (steel and glass fiber reinforced polymer, GFRP) and the configurations of the rebars and steel meshes (single and multiple placements). In terms of load-carrying capacity, the specimens embedded with the GFRP rebars outperform those with the steel rebars and meshes by 14.0%. The post-peak load drop of the blocks with the steel and GFRP rebars is analogous due to distributed axial stresses in the unreinforced concrete region, differing from the abrupt drop observed in the specimens with the steel meshes that intersect the concrete in orthogonal directions. While concrete splitting originates from local tension generated near the axial compression, the location of cracking is dominated by the path of stress trajectories related to the number of rebars, which is not recognized in the case of the meshed specimens. The pattern of the isostatic lines of compression clarifies the development of bursting forces that cause cracking in the concrete. A two-stage analytical model is formulated to predict the magnitude of bursting forces and figure out the effects of several parameters on the response of the end zones. The applicability of existing design expressions is assessed and the need for follow-up research is delineated.

The second part of the report deals with the effectiveness of various reinforcing schemes in the end zones of prestressed concrete bulb-tee girders. The default girder taken from a local transportation agency includes C-bars and spirals, which are intended to control cracking, and three-dimensional finite element analysis is conducted. The formulated models are used to evaluate the breadth of end zones, strain responses, cracking patterns, damage amounts, and splitting forces, depending upon the configuration of the end-zone reinforcement. The number of C-bars is not influential in developing strand stress along the girder. The maximum principal stresses exceed the conventional limit of $h/4$, where h is the girder depth; however, the $3h/4$ limit adequately encompasses the stress profiles, particularly in the web of the girder. The maximum tensile strain in the concrete varies with the elevation of the girder and the inclined strands cause local compression in the C-bars, while spiral strains are independent of the number of bars. By

positioning the C-bars, the vertical strain of the concrete decreases by more than 15.9%, which can minimize crack formation. Whereas the short-term crack width of the girder may not be an immediate concern, its long-term width is found to surpass the established limit of 0.007 in. In this regard, multiple C-bars should be placed to address concerns about undesirable cracking. The splitting cracks in the girder, resulting from the strand angles and eccentricities, can be properly predicted by published specifications within the range of 0.2h to 0.7h, beyond which remarkable discrepancies are observed in comparison with a refined approach. From a practical perspective, two to three No. 6 or No. 7 C-bars spaced 6 in. apart are recommended in the end zones alongside welded wire fabric.

Implementable Outcomes: The research has found that using multiple C-bars is beneficial for controlling end-zone cracks in both the short and long term. Provided that rebar congestion is not a concern during the fabrication of steel cages, two to three No. 6 or No. 7 C-bars spaced 6 in. apart are recommended along with welded wire fabric (W4×W4).

Keywords: bridges; cracking; end zones; girders; prestressed concrete

List of Tables

List of Figures

Table of Contents

Part I: Anchorage Zones Reinforced with Discrete Rebars and Continuous Meshes

I.1. Introduction

Anchorage zones, commonly referred to as end zones, are essential for withstanding prestressing forces in a concrete member. Concentrated axial compression induces local tension in perpendicular directions and causes concrete to split when principal stresses exceed its tensile limit. Adequately designed end zones thus ensure structural integrity for the member under high levels of confining forces. The stress fields of end zones are, however, complex with a variety of force components; as such, fully comprehending how these zones behave is not a straightforward task (Steensels et al. 2019). To mitigate cracking in concrete, detailing end zones is important and reinforcing strategies have gained significance as precasters are reluctant to cast end blocks for economic production (Hiremath et al. 1989). The provisions in the American Association of State Highway and Transportation Officials (AASHTO) Load and Resistance Factor Design (LRFD) Bridge Design Specifications (AASHTO 2020) regarding end-zone reinforcement originated from empirical methods based on experimental results and linear analysis (Burdet 1990; Breen et al. 1994). Hence, premature spalling and bursting cracks often occur (Srinivasan et al. 2020) and transportation agencies are eager to seek solutions that can address those problems. Okumus and Oliva (2013) evaluated crack control techniques via finite element modeling. Of interest were the sequence of strand cutting, cross-sectional area of reinforcing bars, location of draped strands, modification of end-zone reinforcements, and debonding of strands. The area of rebars emerged as the most influential factor with a notable contribution from debonded strands. Steensels et al. (2019) examined the effectiveness of several rebar arrangements and advised placing extra rebars with larger diameters near the end face of members for the purpose of alleviating spalling cracks, in addition to shear stirrups.

Given the frequent inclusion of vertical rebars and welded meshes in precasters' shop drawings, researchers attempted to figure out the efficacy of these reinforcing elements (Tuan et al. 2004; Yao et al. 2021). For convenience, the end zone of prestressed members was simplified to independent concrete blocks under concentric loading on many occasions (Sanders and Breen 1997; He and Liu 2011; Zhou et al. 2017). Hou et al. (2017) developed a numerical model to predict the stress contours of concrete blocks exposed to concentric and eccentric loadings. The profiles of principal stresses changed with the location of axial compression and, as the loaded domain was broadened, the magnitude of bursting stresses abated. The applied loading

commenced to deviate from the vertical axis beyond the quarter length of the loading plate, signifying the importance of near-surface stresses that would govern local tension in the end zones. Zhou et al. (2017) tested concrete specimens reinforced with orthogonally placed steel bars. The ramifications of a loading-plate size varying from 10% to 37.5% of the specimen width were assessed. Bursting cracks appeared above the mid-height of the blocks and progressed in the diagonal direction. The width of the cracks was correlated with the plate size. According to the proposed strut-and-tie model, stress redistributions after concrete cracking were a dominant consideration in establishing force transfer paths. Cui et al. (2019) studied the behavior of rectangular-section concrete with welded meshes. Whereas the resistance of meshes matched that of bent bars, the failure of the welded spots resulted in the brittle failure of the specimens with reduced deformability. Insufficient clarity was stated regarding the meshes' role in ameliorating the cracking response of the sections. Geng et al. (2019) loaded concrete blocks reinforced with welded meshes to characterize splitting and spalling cracks. The meshes efficaciously confined the concrete and raised the axial capacity of the specimens.

In spite of recent endeavors, there still is a dearth of knowledge on the effects of multiple rebar placements and the use of steel meshes; particularly, the fundamental failure characteristics and crack-resisting principles of these reinforcing schemes are limitedly known. Along with it, the potential of alternative reinforcing materials exemplified by glass fiber reinforced polymer (GFRP) composites may be explored to resolve durability matters in concrete structures. This report aims to investigate the performance of multiple discrete rebars and continuous meshes in end zones, as well as to ascertain the feasibility of GFRP rebars that could replace traditional steel rebars. In fact, no research has been reported on the use of such nonmetallic materials for reinforcing end zones. The focus of the study lies on the load-carrying capacity of end zones with those reinforcements and the post-peak behavior of the cracked zones to elucidate full-range responses covering elastic and inelastic states. Through analytical modeling, the development of bursting forces and the repercussions of major parameters are expounded in tandem with design aspects.

I.2. Research Significance

Bursting stresses normal to axial compression prompt cracking in end-zone concrete. Transverse reinforcement is, therefore, required to preclude the irreversible damage of the disturbed region

where beam theory does not apply. Current practices in designing end zones heavily rely upon practitioners' experience and overly conservative design articles (He and Liu 2011). Among many obscure subjects that demand clarification, a thorough understanding of multiple rebars and meshes embedded in concrete takes precedence to offer a rationale for identifying favorable reinforcing systems in end zones with the intention of refining existing provisions. Additionally, the applicability of noncorrosive GFRP rebars needs to be discerned for extending the longevity of prestressed concrete structures. By testing a series of specimens possessing a variable number of rebars and meshes, interactions between the concrete and reinforcing elements are appraised together with post-peak cracking features.

I.3. Test Procedure

The primary segment of the test program consists of material constituents, specimen preparation, and mechanical loading. Monotonic compression is applied to reinforced and unreinforced concrete blocks until failure. Computerized data acquisition systems log their responses and non-contact optical technologies characterize cracking behavior.

I.3.1. Materials

A concrete mixture was designed to achieve a specified compressive strength of f'_c = 3,625 psi with a composition of 22 lb/ft^3 of cement, 11 lb/ft^3 of water, 44 lb/ft^3 of sand, and 66 lb/ft^3 of coarse aggregate. In accordance with ASTM C39 (ASTM 2021), moisture-cured cylinders (4 in. in diameter by 8 in. in length) were tested at 28 days and an average strength of 4,322 psi was obtained. The size of steel and GFRP rebars was No. 3 (diameter = 0.375 in. and cross-sectional area = 0.11 in.^{2}). The designation of the steel rebars was ASTM A572 Grade 60 with a yield strength of f_y = 60 ksi and an elastic modulus of E_s = 29,000 ksi. The surface-indented GFRP rebars, comprising ECR (E-glass corrosion resistant) fibers and a vinylester resin, had a tensile strength of f_{fu} = 145 ksi with an elastic modulus of E_f = 8,700 ksi at a rupture strain of 1.7%. Welded wire meshes were made of galvanized steel strands (ASTM A653) with an opening of 1 in. by 1 in. and a strand cross-sectional area of 0.0013 in.^{2}. The nominal yield strength of the mesh was 36 ksi.

I.3.2. Specimens

A total of 50 specimens were cast with various reinforcing layouts (Fig. I.1). The dimensions of each block were 8 in. by 8 in. by 16 in. The plain concrete without reinforcement served as the control, while others with discrete reinforcement involved one to three steel and GFRP rebars positioned at 2 in. from the top surface (Figs. I.1(a) and (b)). Contrary to the hooked steel rebars, the non-bendable GFRP rebars were straight; nonetheless, premature pull-out failure was not a concern because the rebars were subjected to in-plane shear loading. For those with continuous reinforcement, the meshes covered the interior of the block spanning 6 in. by 12 in. (Fig. I.1(c)). The effective reinforcement ratio of the specimens incorporating the discrete reinforcing elements varied from ρ_{eff} = 0.18% to 0.53%, depending upon the number of embedded rebars, where ρ_{eff} is defined as the total cross-sectional area of the reinforcement divided by the area of the general zone (the product of the member width and the effective member length that is equal to the member width, ACI 2019). The ratio of the specimens with the continuous meshes ranged from ρ_{eff} = 0.014% to 0.043% for one to three layers (only the horizontal strands were taken into account for consistency with the reinforcement ratio of the rebars). Table I.1 enumerates a test matrix showing the types and quantities of the reinforcing rebars and meshes, as well as the number of replications: Plain = no reinforcement, S = steel rebars, G = GFRP rebars, and M = mesh. Every category was iteratively loaded five times. For example, S3-2 means the specimen was reinforced with three steel rebars and was the second repetition of its kind.

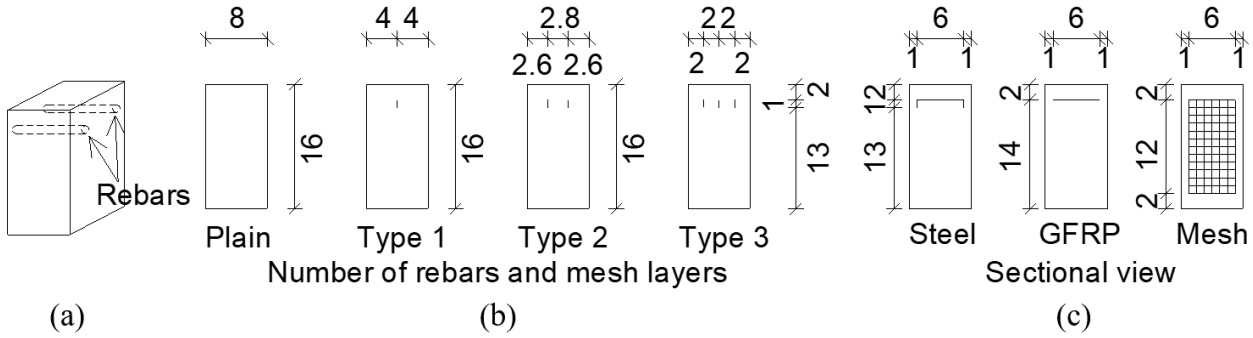

Fig. I.1. Various reinforcing schemes for anchorage zones (units in in.): (a) three-dimensional view; (b) placement of reinforcement; (c) sectional view

Table I.1. Test matrix

ID	Reinforcement		Ultimate load (kip)	
	Type	Number	Ind.	Ave.
Plain-1	N/A	0	73.6	73.6
Plain-2	N/A	0	75.1	
Plain-3	N/A	0	78.2	
Plain-4	N/A	0	64.5	
Plain-5	N/A	0	76.7	
S1-1	Steel rebar	1	65.5	82.7
S1-2	Steel rebar	1	79.8	
S1-3	Steel rebar	1	84.1	
S1-4	Steel rebar	1	93.0	
S1-5	Steel rebar	1	91.0	
S2-1	Steel rebar	2	87.8	86.5
S2-2	Steel rebar	2	91.9	
S2-3	Steel rebar	2	79.5	
S2-4	Steel rebar	2	82.3	
S2-5	Steel rebar	2	90.9	
S3-1	Steel rebar	2	92.5	91.6
S3-2	Steel rebar	2	89.6	
S3-3	Steel rebar	2	96.3	
S3-4	Steel rebar	2	88.6	
S3-5	Steel rebar	2	90.6	
G1-1	GFRP rebar	1	95.2	93.1
G1-2	GFRP rebar	1	82.3	
G1-3	GFRP rebar	1	101.0	
G1-4	GFRP rebar	1	88.5	
G1-5	GFRP rebar	1	98.8	
G2-1	GFRP rebar	2	101.0	97.1
G2-2	GFRP rebar	2	86.2	
G2-3	GFRP rebar	2	102.4	
G2-4	GFRP rebar	2	96.4	
G2-5	GFRP rebar	2	99.4	
G3-1	GFRP rebar	3	92.2	98.3
G3-2	GFRP rebar	3	99.6	
G3-3	GFRP rebar	3	101.1	
G3-4	GFRP rebar	3	98.7	
G3-5	GFRP rebar	3	99.7	
M1-1	Steel Mesh	1	73.6	79.6
M1-2	Steel Mesh	1	71.0	
M1-3	Steel Mesh	1	82.5	
M1-4	Steel Mesh	1	88.3	
M1-5	Steel Mesh	1	82.6	
M2-1	Steel Mesh	2	86.9	83.6
M2-2	Steel Mesh	2	80.1	
M2-3	Steel Mesh	2	88.9	
M2-4	Steel Mesh	2	81.5	
M2-5	Steel Mesh	2	80.4	
M3-1	Steel Mesh	3	89.5	85.7
M3-2	Steel Mesh	3	86.7	
M3-3	Steel Mesh	3	85.1	
M3-4	Steel Mesh	3	85.1	
M3-5	Steel Mesh	3	82.1	

I.3.3. Experimental Protocol

As mentioned earlier, five cylinders were loaded to determine the 28-day compressive strength of the hardened concrete mixture (Fig. I.2(a)). The prepared blocks were placed on top of a circular plate (Fig. I.2(b)) and a concentric load was applied at a rate of 1 0.0394 in./min through a rectangular steel bearing plate (2 in. wide by 3 in. long by 1.2 in. thick). A load cell and a linear potentiometer recorded the load and displacement of the specimens, respectively. To study the progression of cracking, digital image correlation (DIC) was employed with a 5-megapixel high-resolution camera and a quad-core computer for processing scanned data.

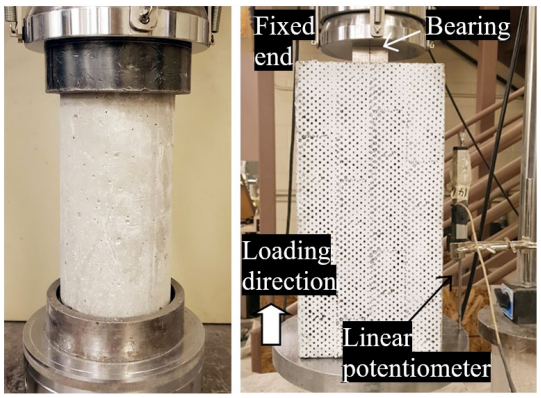

(a) (b)

Fig. I.2. Test protocol: (a) concrete cylinder; (b) anchorage zone element

I.4. Results

Findings from the experimental program are delineated with an emphasis on the axial strength of concrete members with and without reinforcing elements, the influence of discrete rebars and continuous meshes, failure aspects, and crack patterns. A comprehensive analysis is undertaken to gauge the practicality of assorted reinforcing schemes in end zones.

I.4.1. Capacity

The load-carrying capacities of the individual specimens are listed in Table I.1, depending upon the type of reinforcement, and their average values are charted in Fig. I.3(a). The difference between the specimens with the steel rebars and meshes was 4.5%, whereas the GFRP-reinforced concrete blocks revealed higher capacities than others by up to 15.9%. These observations indicate that the spread mesh configuration was comparable to the case of the discrete rebars,

notwithstanding the differences in reinforcement ratios (0.043% vs. 0.53% for the blocks with three mesh layers and rebars, respectively), and that the nonmetallic composite rebars were a feasible alternative to the steel rebars for reinforcing anchorage zones. Figure I.3(b) demonstrates the enhanced capacities of the reinforced blocks against the plain ones (increase ratio = reinforced/unreinforced). With an increase in the number of steel rebars and meshes, the discrepancy between the reinforced and plain specimens went up; for instance, the capacity ratios of the S1 and S3 categories with one and three rebars were 1.12 and 1.24, respectively. However, the ratio of the GFRP-reinforced blocks remained nearly constant with the number of rebars: 1.27, 1.32, and 1.33 for one, two, and three rebars, respectively. This is attributed to the fact that the concrete dominated the failure of the specimens and the multiple GFRP rebars did not remarkably impinge upon the reinforcing mechanism; scilicet, the concrete component disintegrated before fully utilizing the high strength of the composite rebars (to be revisited in the failure mode section).

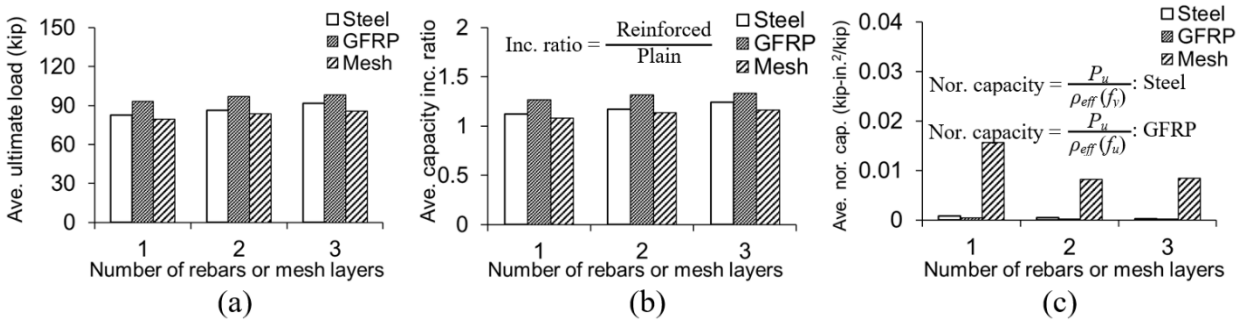

Fig. I.3. Load-carrying capacity: (a) average ultimate load of test specimens; (b) average increased capacity compared with control capacity; (c) average normalized capacity

Figure I.3(c) describes the capacities of the specimens normalized by the effective reinforcement ratio (ρ_{eff}) and the strength of the rebar and mesh (f_y for steel and f_u for GFRP). This analysis considers diverse material properties and reinforcing schemes, contributing to understanding the functionality of these specific constituents. When the number of rebars and mesh layers was incremented, the normalized capacities declined and the steel meshes outperformed other options. Consequently, deploying such uniformly distributed reinforcing elements with an optimal cross-sectional area is a viable solution for anchorage zones, while another possibility could be to sequentially place multiple discrete rebars in the longitudinal

direction of the zones. Even though the high strength of GFRP (f_{fu} = 145 ksi) lowered the normalized capacities (Fig. I.3(c)), it does not necessarily mean that the performance of the composite was worse: smaller cross-sectional areas of the GFRP rebars can achieve equivalent load-bearing capacities to the steel rebars, as depicted in Fig. I.3(a).

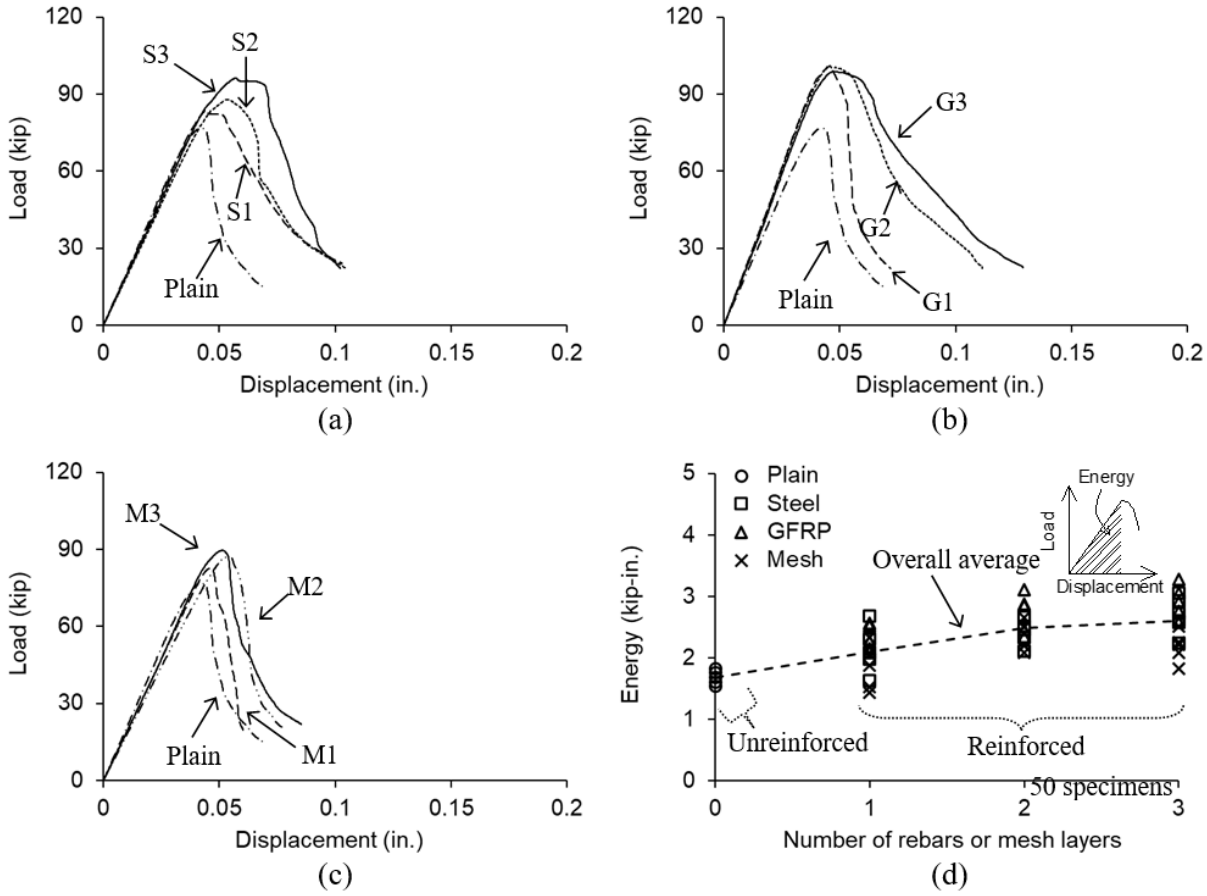

Fig. I.4. Load-displacement: (a) steel rebars; (b) GFRP rebars; (c) steel meshes; (d) energy dissipation up to peak loads

I.4.2. Load-Displacement

The load-displacement behavior of representative specimens is graphed in Figs. I.4(a) to (c). For the blocks with and without steel rebars (S1 to S3 and Plain, Fig. I.4(a)), the response ascended linearly until reaching peak loads and the number of embedded rebars affected the ultimate loads. The moderate load drops in the post-peak region imply that the applied axial stresses were distributed within the concrete (to be elaborated in the modeling section) and the rebars resisted the splitting of the concrete, known as the crack-bridging mechanism (Drar and Matsumoto

2016). The specimens with the GFRP rebars manifested analogous responses (Fig. I.4(b)). Although the aforementioned independence of the ultimate loads from the number of rebars was evident, it was influential for the post-peak behavior. A possible explanation is that the indented surfaces of the multiple GFRP rebars improved mechanical interlock, thereby delaying the opening of the cracked concrete. The specimens with the meshes exhibited a parallel predisposition (Fig. I.4(c)); however, owing to the vertical arrangement of the reinforcement, the post-peak slopes decreased steeply relative to those with the horizontal reinforcing elements (Figs. I.4(a) and (b)). Figure I.4(d) provides the dissipated energy of the specimens up to the peak loads, calculated by integrating the area under the load-displacement curves (Fig. I.4(d), inset). Despite scattering, the reinforced blocks showed higher energy dissipation than the plain blocks and the energy variation tended to stabilize after the addition of two rebars and mesh layers. For that reason, ensuring an adequate number of rebars and mesh layers is salient for concrete members in the end zone.

I.4.3. Failure Mode

Plotted in Fig. I.5 is the failure mode of the specimens. Regarding plain concrete (Fig. I.5(a)), the concentrated compression force induced local tension beneath the loading plate, resulting in a conspicuous separation of the cracked surfaces and ultimately leading to the splitting of the specimen. In line with the control specimen, the cracking of the blocks with one and two steel rebars initiated below the loading point and intersected the rebars (S1 and S2, Fig. I.5(b)). A combination of static friction and chemical adhesion enabled those rebars to counteract the horizontal displacement of the concrete (Chiriatti et al. 2019). Contrarily, crack formation in the three-rebar specimen (S3, Fig. I.5(b)) shifted away from the loading point because the dispersed rebars altered the path of stress trajectories. Across the board, inclined cracks were not detected due to the absence of eccentricity in loading. The failure pattern of the GFRP-rebar specimens was akin to their steel counterparts in the context of crack progression (G1 and G2, Fig. I.5(c)) and the formation of deviated cracks in the block containing three rebars (G3, Fig. I.5(c)). The cracking adjacent to the quarter points of the upper region in the G3 specimen reaffirms the distributed stresses stemming from the presence of the three rebars. Furthermore, the consistent cracking of S3 and G3 with the ultimate loads higher than those of the plain concrete (91.5 kips and 98.3 kips vs. 73.6 kips in Table I.1) adduces the potential of GFRP rebars as reinforcing

elements in end zones. On the specimens with the meshes (Fig. I.5(d)), vertical cracks were observed like others; by contrast, the deviated cracking was not seen in the case with three-mesh layers (M3). This illustrates the possibility of coupling meshes and rebars perpendicular to the loading direction in practice (hybrid reinforcing), so as to effectively distribute applied stresses across the end-zone concrete.

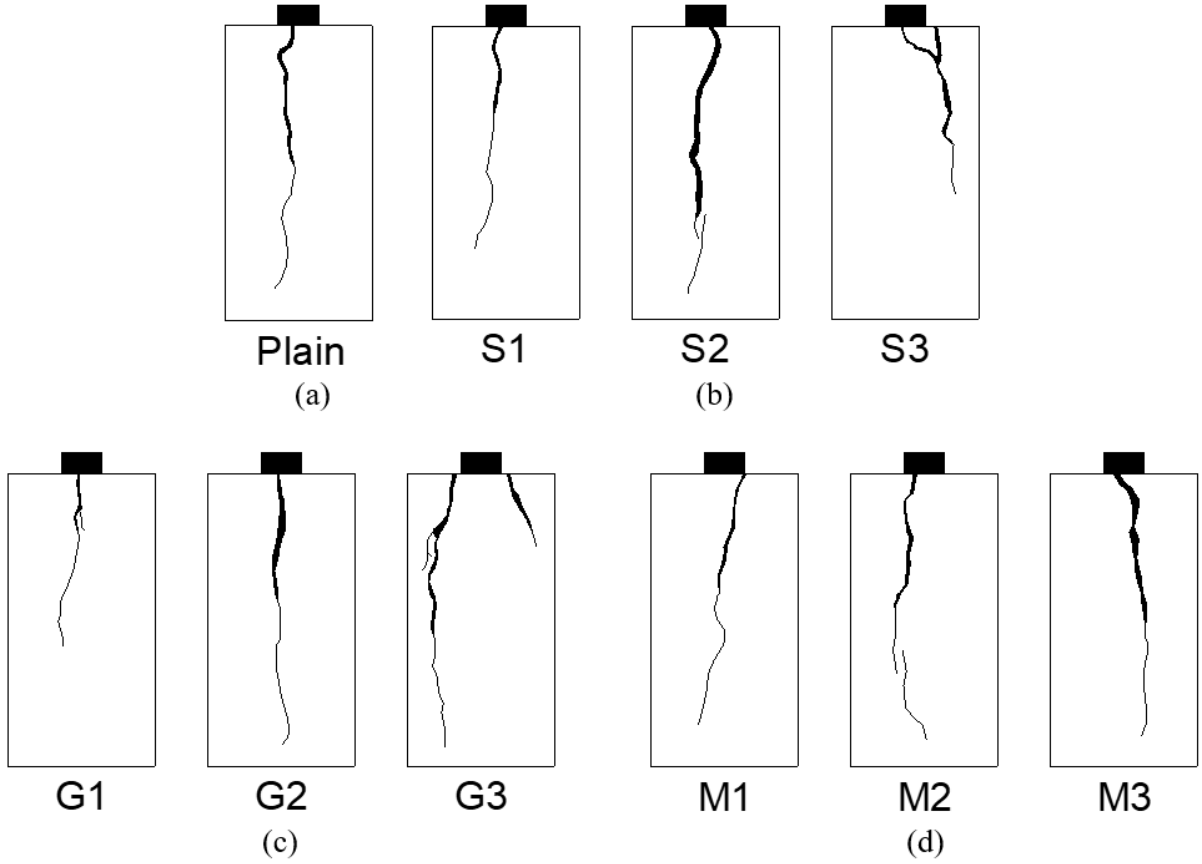

Fig. I.5. Failure mode: (a) Plain; (b) steel rebars; (c) GFRP rebars; (d) steel meshes

I.4.4. Evolution of Cracking

The sequential images of concrete-cracking throughout the post-peak range of the specimens are pictured in Fig. I.6. It should be noted that the variation in color contours does not convey technical information since they merely display the relative elevations of the scanned texture. With the axial load continuing beyond the capacity of the Plain specimen (Fig. I.6(a)), a crack initiated underneath the bearing plate and propagated orthogonally to the principal compressive stress trajectories, which is well documented in deep-beam testing (Mukhtar and Deifalla 2023). As the vertical crack advanced, tensile stresses across it accelerated the opening of the concrete: the extended crack may serve as an indirect indicator of diminished stress transfer within the concrete. The cracking appearance in the S1 and G2 specimens was similar to that in the Plain specimen (Figs. I.6(b) and (c)); nonetheless, their cracking tendencies varied. The low modulus of the non-metallic reinforcement (E_f = 8,700 ksi for GFRP vs. E_s = 27,000 ksi for steel) was responsible for the expanded crack opening in the GFRP specimen (Fig. I.6(c)). From an

equilibrium standpoint, the tensile forces of the steel and GFRP rebars were balanced with the compression resistance of the block in the transverse direction until splitting failure took place. The cracking of the M3 specimen steadily grew with narrow openings (Fig. I.6(d)), underscoring the potential advantages of placing continuous meshes in end zones.

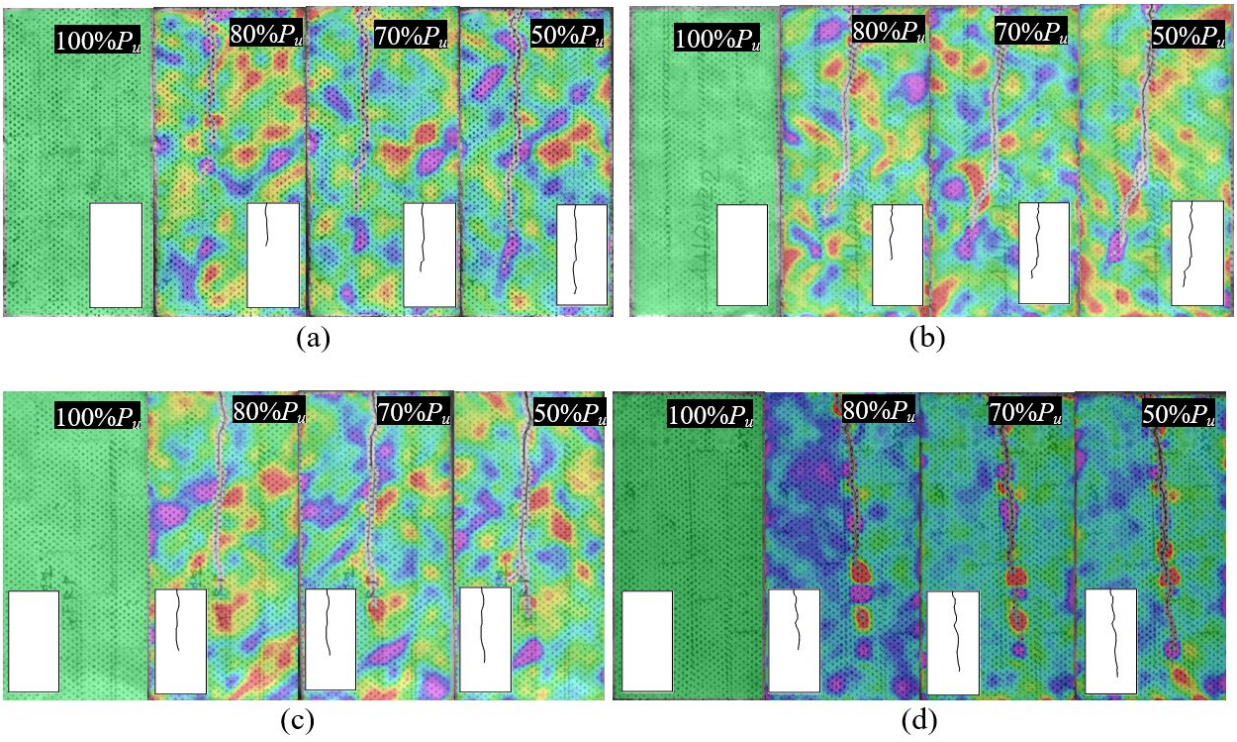

Fig. I.6. Progression of cracking depicted by digital image correlation (percentages indicate post-peak load levels): (a) Plain; (b) S1; (c) G2; (d) M3

Figures I.7(a) to (c) show the cracked areas of the specimens in the post-peak domain, quantified by image processing software. To assist in discussions, the average cracked areas of the test categories were expressed as a percentage relative to the entire area of the concrete block in the loading direction. Differences were found between the responses of the Plain and the S and G specimens; specifically, the increased number of steel and GFRP rebars corresponded to elongated crack percentages (Figs. I.7(a) and (b)). This can be accounted for by the fact that the reinforced specimens with higher capacities (Table I.1) incurred more concrete cracking. In the M specimens (Fig. I.7(c)), the crack percentages were markedly reduced because of the distributed mesh layout across the concrete section: consistent with the foregoing specimens, the increased load-bearing capacities of the M1 to M3 specimens were linked to more cracking. The

overall post-peak behavior of the S, G, and M specimens is visually assessed in Fig. I.7(d) on the basis of their characteristic areas, which were attained by numerically integrating the area under the post-peak load vs. crack percentage curves for the examination of cracking tolerance up to $0.5P_u$. The tolerance of the rebar specimens (S and G) was aligned; however, the mesh specimens (M) averaged less than 65%. To accommodate the uneven ultimate loads of the specimens, the characteristic areas were normalized by the capacities (Fig. I.7(e)). The specimens with multiple steel rebars underwent large crack areas, with the GFRP-rebar and steel-mesh specimens having lesser degrees of cracking.

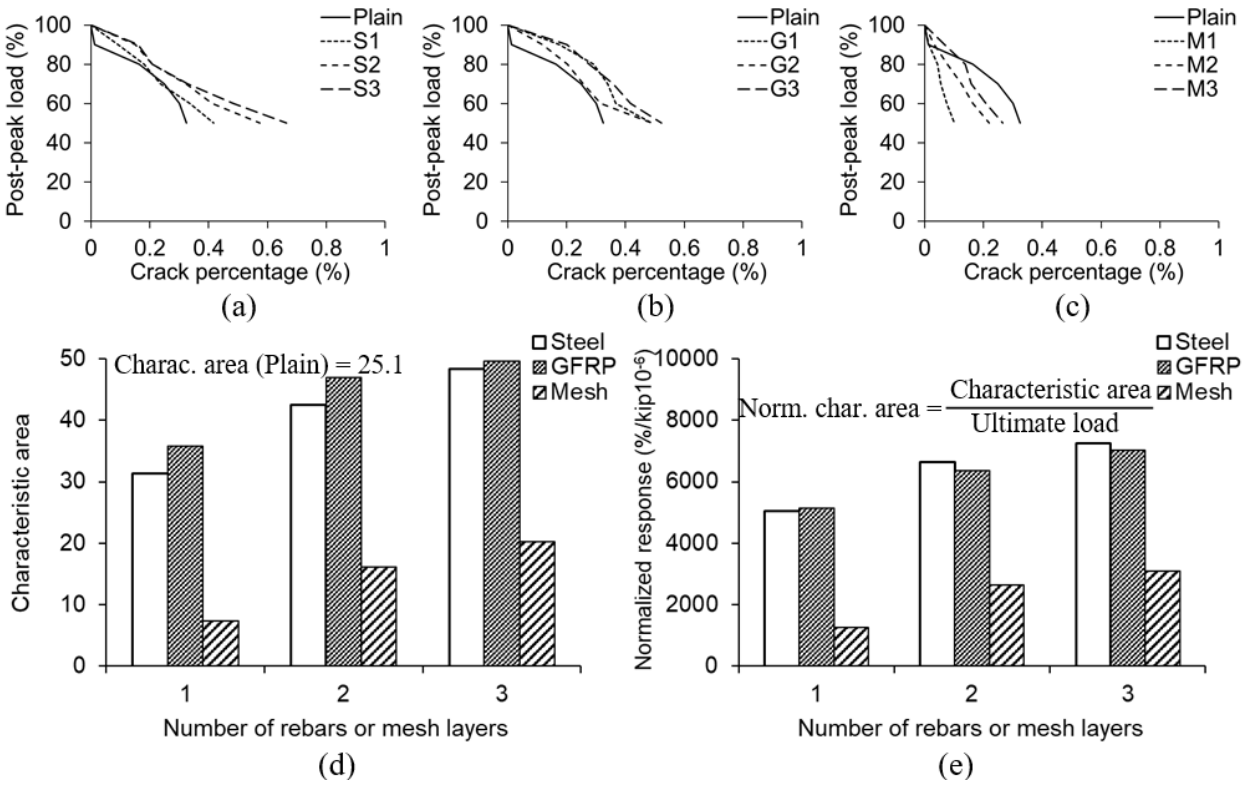

Fig. I.7. Crack analysis (average values): (a) steel rebars; (b) GFRP rebars; (c) steel meshes; (d) characteristic area; (e) normalized response

I.5. Analytical Modeling

A two-stage modeling approach is developed to predict reinforcement responses and bursting forces in the experimental end-zone specimens. The efficiency of discrete rebars and continuous meshes is detailed and the relevance of a nodal stress limit stipulated in ACI 318 (ACI 2019) is

evaluated. Sensitivity analysis explicates the implications of varying parameters for the behavior of the specimens.

I.5.1. Description

Figures I.8(a) and (b) portray the concentrically loaded block models before and after cracking, respectively. The succeeding assumptions were made to facilitate the formulation of the analytical models, which are customary in the theory of elasticity and the strut-and-tie method (Ugural and Fenster 1995; He and Liu 2011; ACI 2019; ACI 2021)

a) In-plane loading is exerted on the control and reinforced concrete blocks
b) St. Vernant's principle is valid within the disturbed region of the specimens
c) Reinforcement becomes effective once cracking occurs in the concrete
d) The distribution of bursting stress along the specimen's height is represented by a resultant force
e) The location of the resultant bursting force remains unchanged after concrete cracking

The size of the specimens was appropriate for fully generating a bursting stress profile; that is, the length of the blocks was longer than their width (aspect ratio > 1.0, Sahoo et al. 2009).

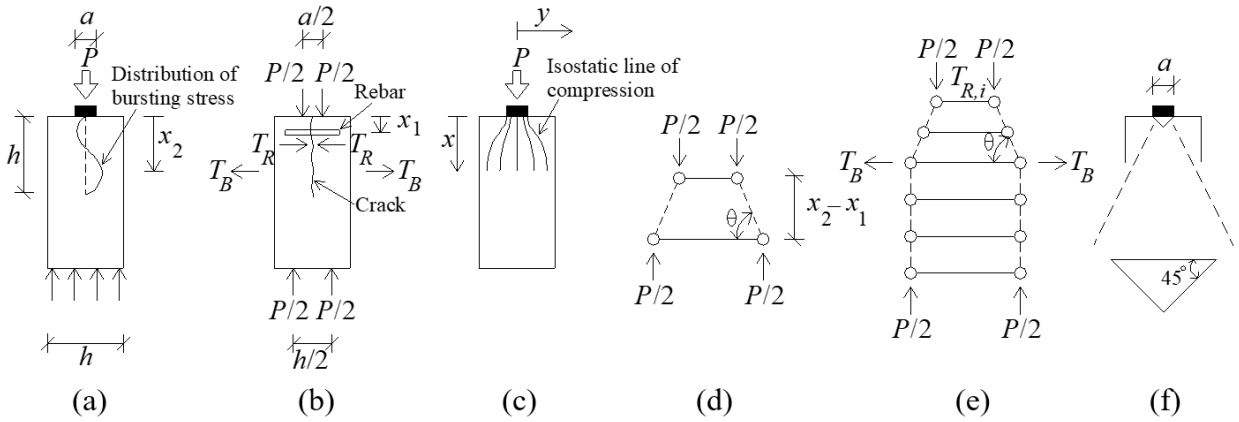

Fig. I.8. Model description: (a) before cracking (Stage I); (b) after cracking (Stage II); (c) isostatic lines of compression; (d) strut-and-tie for steel and GFRP rebars; (e) strut-and-tie for steel meshes; (f) nodal zone

Stage I—The first stage of the model is concerned with the specimens until the concrete cracks. The isostatic lines of compression (y, Fig. I.8(c)), initially proposed by Guyon (1953), and the transverse stress of the concrete along the loading direction ($\sigma_T(x)$) may be expressed as (He and Liu 2011)

$$y = y_i\left[\frac{(h-a)x^2}{h^3}\left(\frac{3}{h^2}x^2 - \frac{8}{h}x + 6\right) + \frac{a}{h}\right] \tag{I.1}$$

$$\sigma_T(x) = -\frac{3(h-a)P}{2h^4 t}\left(3x^2 - 4hx + h^2\right) \tag{I.2}$$

where y_i is the vertical coordinate of the isostatic line of compression at $x = h$; h and a are the width of the specimen and the loading plate, respectively; and P is the concentric load. On account of difficulties in measuring the bursting force of the specimen (Sahoo et al. 2009), Eq. I.3 may be used to estimate the force (T_B) up to the cracking of the concrete (Oluokun 1991; He and Liu 2011)

$$T_B = \int_{h/3}^{h} \sigma_T(x)\,t\,dx = \frac{2}{9}P\left(1 - \frac{a}{h}\right) \tag{I.3}$$

$$P_{cr} = \frac{2ht}{(1 - a/h)}f_t \tag{I.4}$$

$$f_t = 0.214\left(f_c'\right)^{0.69} \tag{I.5}$$

where t is the thickness of the specimen; P_{cr} is the cracking load; and f_t is the splitting strength of the concrete.

Stage II—Once the load surpasses the cracking load ($P \geq P_{cr}$), the specimen cracks and the model shifts to the second stage as per the concept of strut-and-tie. For the blocks with the steel and GFRP rebars (Fig. I.8(d)), force equilibrium leads to

$$C = \frac{P}{2\sin(\theta)} \tag{I.6}$$

$$T_B = \frac{P}{2}\cot(\theta) \tag{I.7}$$

$$\theta = \arctan\left(\frac{(h-a)}{4(x_2 - x_1)}\right) \tag{I.8}$$

where C is the force in the compression strut; θ is the force component angle in degrees; and x_2 and x_1 are the characteristic positions of the reinforcement (Figs. I.8(a) and (b)). When the steel meshes are embedded in the specimen (Fig. I.8(e)), the horizontal strands counteract the bursting of the concrete.

Force in reinforcement—The rebar force (T_R) may be equated with the spalling force (T_{sp}) and acquired by $T_R = T_{sp} = 0.02P$, as prescribed in ACI 318 (ACI 2019), in conjunction with Eqs. I.3 and 7

$$T_R = \begin{cases} \dfrac{0.09}{\left(1-\dfrac{a}{h}\right)} T_B & \text{before cracking} \\ \dfrac{0.04}{\cot\theta} T_B & \text{after cracking} \end{cases} \tag{I.9}$$

The mesh grids outside the general zone do not interact with horizontal forces in light of the second assumption given previously, which is reasonably acceptable as shown in Fig. I.6(d). The spalling force is then assumed to be evenly distributed among the individual strands associated with the general zone, which is archetypal in strut-and-tie models

$$\sum_{i=1}^{m} T_{R,i} = T_{sp} \tag{I.10}$$

$$m = \frac{h - x_1}{s} + 1 \tag{I.11}$$

where $T_{R,i}$ is the force of the i^{th} strand; m is the number of the strands in the general zone, including the one at the boundary; and s is the aperture size of the grid.

Nordal resistance—The nodal stress of the concrete underneath the loading plate (σ_{node}, Fig. I.8(f)) may be calculated by

$$\sigma_{node} = \frac{P}{A_{node}} \le k_1 f_c' \tag{I.12}$$

$$A_{node} = \sqrt{\frac{1}{2}} a \cos\left(45^\circ - \theta\right) t \tag{I.13}$$

where k_1 is the limit coefficient for design (k_1 = 0.68 for a compression-tension-compression node in the strut-and-tie model, ACI 2019).

I.5.2. Predicted Response

Plain specimen—Figure I.9(a) renders the isostatic lines of compression in the upper part of the symmetric concrete block. The curvilinear trajectory of the isostatic lines gradually rose beyond approximately x = 2 in. and stabilized after x = 6 in. This conformational development points out that the slanted lines were engaged with non-axial force components, creating bursting forces that could split the concrete. As shown in Fig. I.9(b), the resultant bursting force (T_B, Eq. I.3) increased linearly with the applied load (P) up to failure. The theoretical cracking load of P_{cr} = 64.1 kips was 13% lower than the average ultimate load of P_u = 73.6 kips. The transition from compressive to tensile stresses is visible in Fig. I.9(c). The transverse stress in the tenzon zone ($\sigma_1(x) > 0$) precipitated the cracking of the plain specimen and the splitting failure was predicted at f_t = 323.4 psi. Significant nonlinearity was apparent between the nominal ($\sigma_{nominal} = P/(ta)$) and the transverse ($\sigma_1(x)$) stresses (Fig. I.9(d)). The maximum transverse stress in tenson was 35.9% of the nominal stress at x = 5.2 in., where the resultant bursting force (T_B) was located.

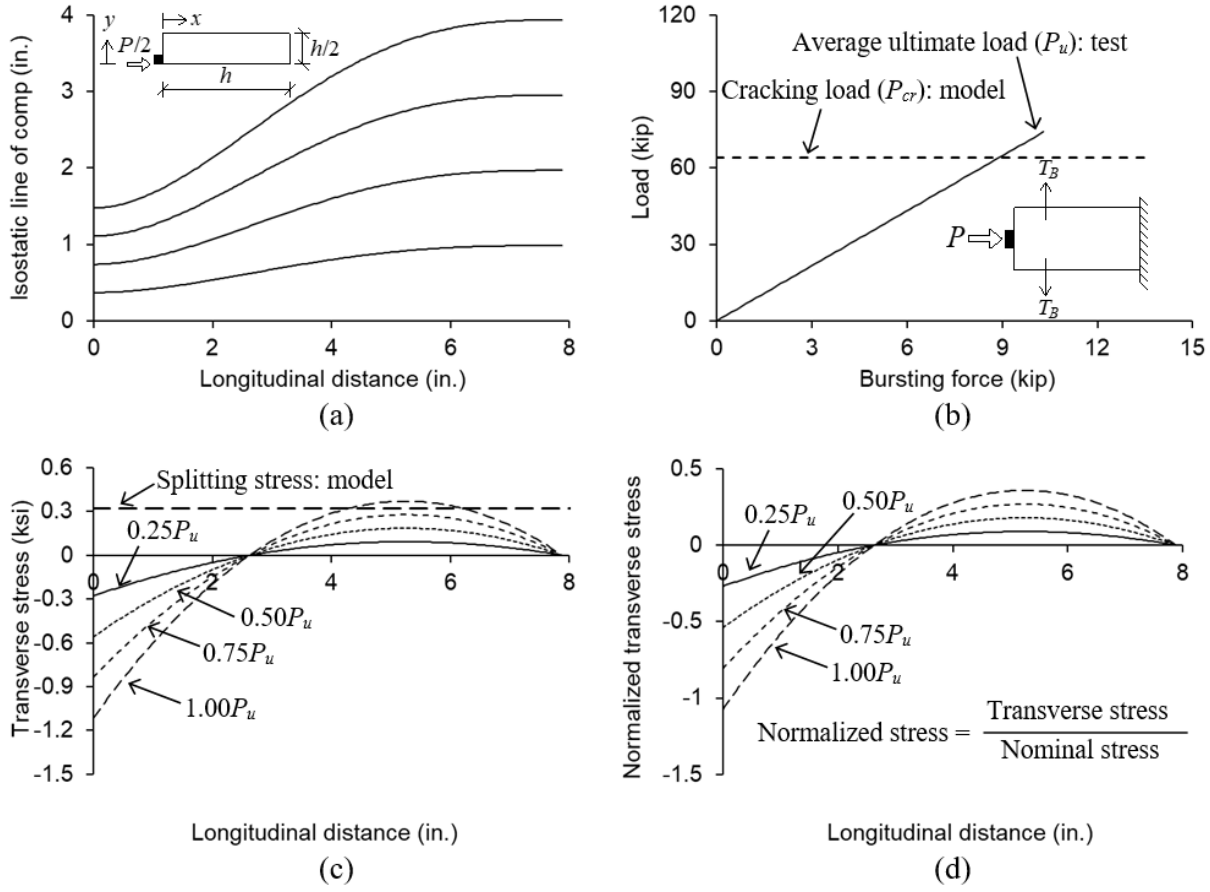

Fig. I.9. Plain specimen: (a) isostatic line of compression; (b) bursting force; (c) transverse stress; (b) normalized transverse stress

Reinforced specimen—The behavior of the specimens with the rebars and meshes is provided in Fig. I.10. Prior to the cracking of the concrete ($P \leq P_{cr}$), the response of the plain and reinforced blocks was identical (Fig. I.10(a)); however, a remarkable increase in the bursting force was computed as soon as the specimen cracked and the force continued to elevate until the load-carrying capacity of the S1 specimen was reached (P_u = 82.7 kips). The reduced slope of the load vs. bursting force curve after cracking (85.9 kips $\leq T_B \leq$ 110.4 kips) is ascribed to the internal forces in the uncracked concrete being directly transferred through the narrow compression struts. Shown in Fig. I.10(b) is the stress of the steel rebars normalized by the yield strength of f_y = 60 ksi. When the number of rebars was increased, the normalized stress decreased, especially between the one- and two-rebar cases. This supports the fact that placing at least two rebars perpendicular to the loading direction is beneficial for lowering stresses, which would preserve the integrity of the end zone exposed to substantial mechanical and

environmental distress over the long term. With the inclusion of the GFRP rebars (Fig. I.10(c)), the normalized stresses were noticeably lessened due to the high tensile strength of f_{fu} = 145 ksi and it confirms the extended service life of composite-reinforced concrete members (Esmaeili et al. 2020). Even if the magnitudes of the normalized stresses were intended to compare the axial resistance of the rebars solved from the strut-and-tie method, the propensity can be valid under shear loading because the shear strength of the steel rebars is proportional to their axial strength pursuant to the maximum shearing stress theory (Ugural and Fenster 1995), which is also acceptable for the GFRP rebars (Sawpan 2016). Relative to the rebar specimens, the ones reinforced with the meshes demonstrated considerable stress levels as a result of the strands' small cross-sectional area (Fig. I.10(d)); in view of this, attention should be paid to the size and number of such interconnected strands to avert issues anticipated during the functional period of the end zone.

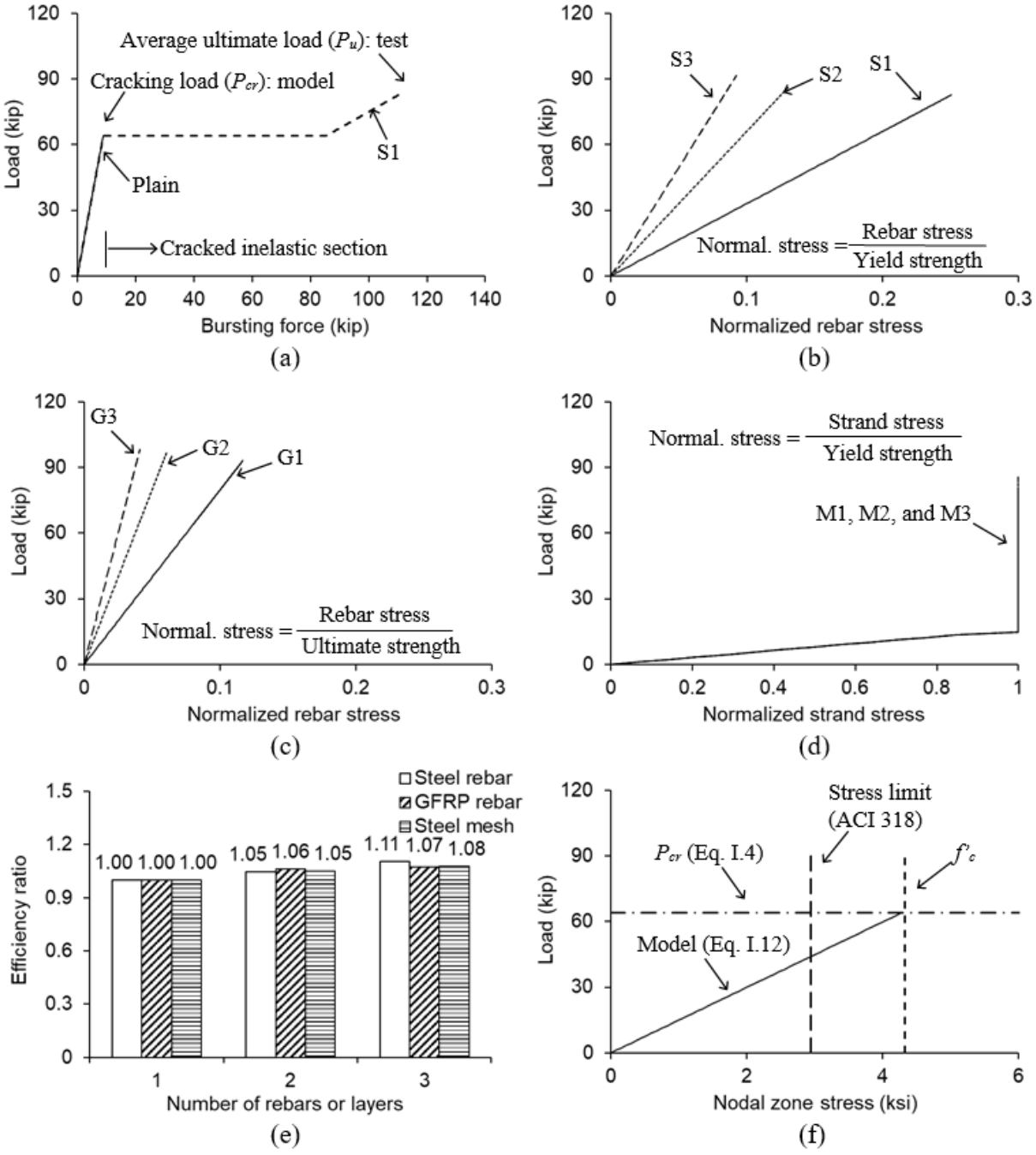

Fig. I.10. Specimen with reinforcement: (a) bursting force; (b) normalized stress of steel rebars; (c) normalized stress of GFRP rebars; (d) normalized stress of steel meshes; (e) efficiency ratio; (f) nodal stress up to cracking

The efficiency of placing multiple rebars and meshes may be examined by Eq. I.14

$$\psi = \frac{T_R(n)}{T_R(1)} \tag{I.14}$$

where ψ is the reinforcement efficiency ratio; $T_R(n)$ is the bursting resistance force with n rebars and mesh layers; and $T_R(1)$ is the resistance force with one rebar and mesh layer. The steel rebars and meshes benefited from increasing the number of reinforcing elements (Fig. I.10(e)); on the other hand, the efficiency of the multiple GFRP rebars was nearly constant with only a marginal impact from adding more rebars, as explained earlier. Figure I.10(f) exhibits the growth of the nodal zone stress under the loading plate (Eq. I.12). At the cracking of the specimens when the elastic concrete body transformed into the inelastic truss-like morphology in the strut-and-tie framework, the predicted maximum stress (σ_{node} = 4,279 psi) was close to the compressive strength of the concrete (f'_c = 4,322 psi) and was 45.3% higher than the ACI stress limit of 2,944 psi. The proposed two-stage modeling approach can thus be conservatively applied in practice, aligning with the widely accepted notion that strut-and-tie models set a lower bound for the capacity of reinforced concrete members (El-Metwally and Chen 2017).

I.5.3. Parametric Study

The sensitivity of the end-zone specimens to crucial parameters is highlighted in Fig. I.11. The default properties of the specimens were those of the Plain and S1, G1, and M1 blocks, unless otherwise specified. When the concrete strength (f'_c) was increased, the cracking load (P_{cr}) of the plain and reinforced specimens went up linearly (Fig. I.11(a)). As far as geometric properties are concerned, the variation of the cracking load was more susceptible to the loaded area ratio (a/h, Fig. I.11(b)) than the thickness ratio (t/h, Fig. I.11(c)). The reason is that the increased a/h distributed the applied load within the uncracked concrete, allowing the specimen to carry a greater load before the onset of cracking. Figures I.11(d) to (f) clarify the consequences of adjusting the geometric properties (a/h and t/h) and loading angle (θ) on the bursting force of the uncracked specimens subjected to a typical service load of $0.3P_{cr}$. In contrast to the t/h and θ situations, the bursting force was contingent upon the a/h ratio because the elastic approach merely handles in-plane stresses (Eq. I.3). After cracking, these trends reshaped and larger force values were predicted from the inelastic strut-and-tie model (Figs. I.11(g) to (i)). Given that the

failure loads of the steel- and GFRP-rebar specimens differed (Table I.1), the applied load level was taken to be the average ultimate load of the Control specimens (P_u = 73.6 kips, Plain) for comparison purposes. The increased cracking load with the enlarged a/h ratio (Fig. I.11(b)) brought about an appreciable rise in the bursting force after cracking (Fig. I.11(g)); on the contrary, the effect of the t/h ratio was virtually none (Fig. I.11(h)). Misinterpretation of these findings should be avoided to prevent the misconception that the surged bursting force meant expedited failure, as the ability to resist a high bursting force is actually enhanced by retarded cracking; additionally, the modification of the t/h ratio is not insignificant since the widened aspect ratio of the end zone is inherently advantageous for stress control. An exponential drop in the bursting force was noticed with the larger angle (Fig. I.11(i)) owing to the reduced horizontal force component (Fig. I.8(d)). The stress of the steel and GFRP rebars declined with the increased effective reinforcement ratio in a like manner (Figs. I.11(j)), while the magnitude of the mesh stress was more pronounced up to the point of yielding (Fig. I.11(k)). The size of the grid openings played a major role in reinforcement stress (Fig. I.11(l)); accordingly, selecting an appropriate mesh size is a critical factor in practice.

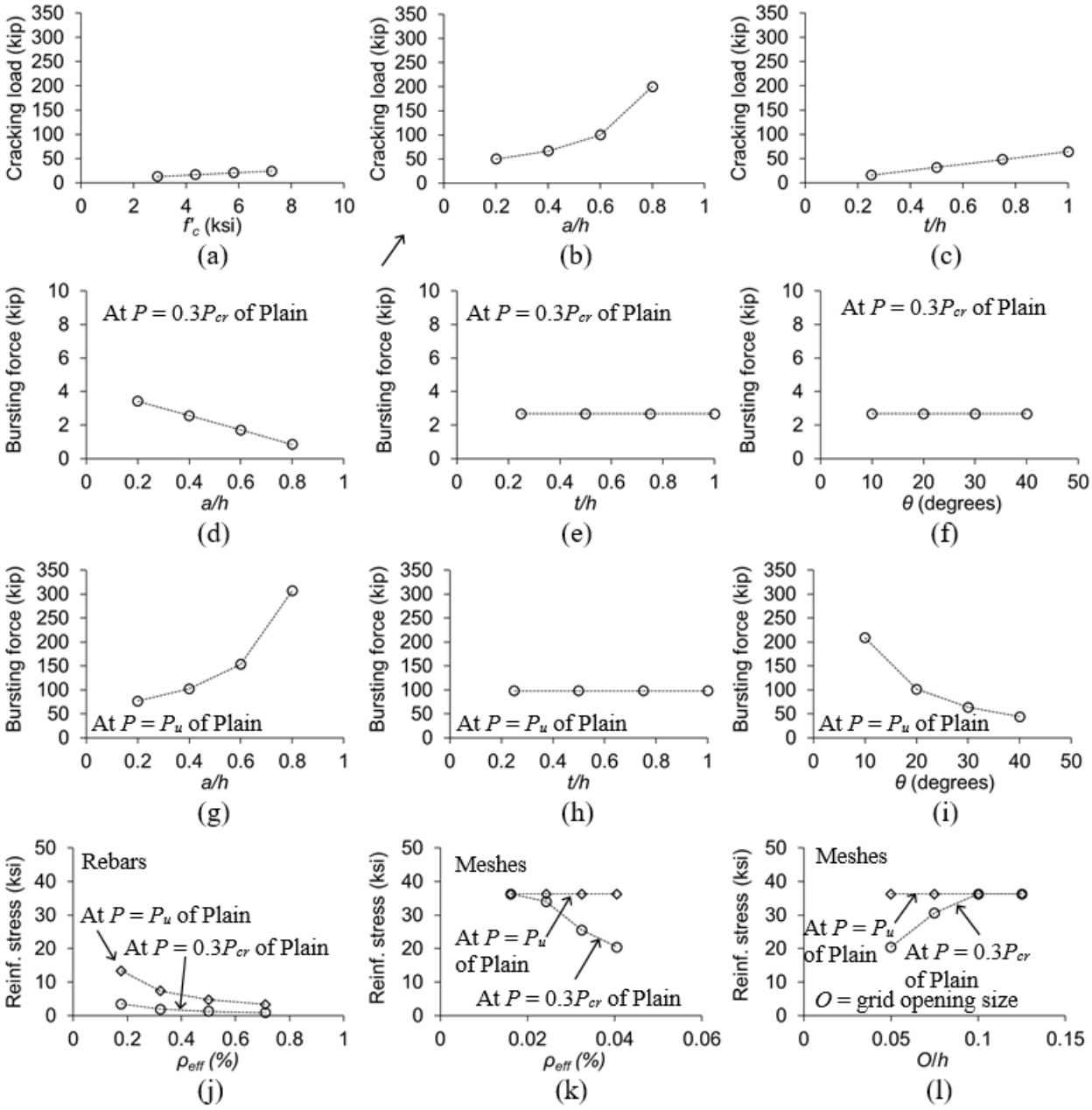

Fig. I.11. Parametric study: (a) cracking load with f'_c; (b) cracking load with a/h; (c) cracking load with t/h; (d) bursting force before cracking with a/h; (e) bursting force before cracking with t/h; (f) bursting force before cracking with θ; (g) bursting force after cracking with a/h; (h) bursting force after cracking with t/h; (i) bursting force after cracking with θ; (j) rebar stress with ρ_{eff}; (k) mesh stress with ρ_{eff}; (l) mesh stress with O/h

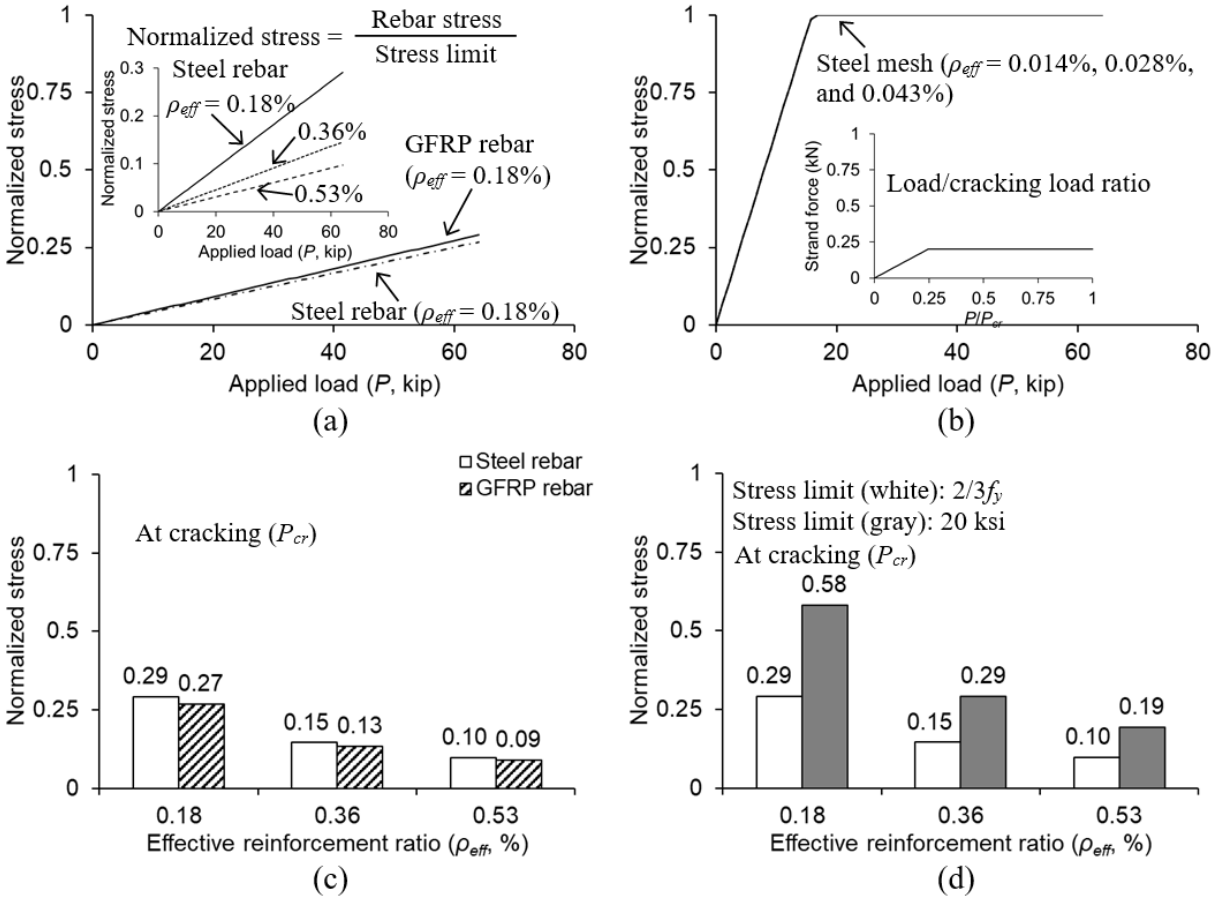

Fig. I.12. Design consideration: (a) discrete rebars; (b) continuous mesh layers; (c) comparison between steel and GFRP rebars; (d) alternative stress limit for steel rebars

I.5.4. Design Perspectives

The stress limits of the steel and GFRP rebars were assigned to be $2/3f_y$ and $0.005E_f$ in compliance with ACI 318 (ACI 2019) and ACI 440.11 (ACI 2022), respectively, and the calculated stresses were normalized for assessments (Fig. I.12(a)). The rationale for adopting these limits was to preclude cracking in steel-reinforced concrete (ACI 2019) and to obviate the premature rupture of GFRP rebars (ACI 2022). The evolution of the normalized stresses for the steel and GFRP rebars was alike, modulated by the effective reinforcement ratio (Fig. I.12(a), inset). The stress of the steel meshes was normalized by the yield strength of f_y = 36 ksi, attributable to the scarcity of specific limits in published specifications. The thin mesh strands with effective reinforcement ratios from 0.014% to 0.043% experienced yielding at an applied load of P = 16.9 kips, which is equivalent to $0.26P_{cr}$ (Fig. I.12(b)). This fact corroborates the importance of mesh configurations as a reinforcing element for end zones, which warrants

extended research to figure out suitable mesh details alongside a stress limit in conformity with those of the rebars. Figure I.12(c) shows the mutual relevance of the steel and GFRP rebars at the cracking load of P_{cr} = 64.1 kips, substantiating the validity of both reinforcement types for end-zone applications. The effectiveness of the empirical stress limit of 20 ksi for non-prestressed end-zone reinforcement, frequently employed by practitioners (Nawy 2009), is appraised in Fig. I.12(d). Even with the conservative approach, the normalized stress of the steel rebars was maintained less than 60% of the limit; hence, the empirical limit can justifiably be permitted for controlling stress levels in end zones.

I.6. Summary and Conclusions

This report has discussed the behavior of anchorage zones with discrete rebars and continuous meshes. Under monotonic compression, 50 specimens were tested to investigate the effects of different reinforcing types and materials on the capacity, cracking, and failure of the end zones. The practicality of employing nonmetallic GFRP reinforcement was of interest. The two-stage analytical model, formulated with elastic equations and the strut-and-tie method, predicted bursting forces for the plain and reinforced specimens before and after concrete cracking. Parametric studies accounted for significant variables affecting the cracking loads, bursting forces, and reinforcement stresses of the end zones. In supplementary fashion, design aspects were articulated to evaluate the adequacy of existing expressions and to identify the necessity for new provisions dealing with the unconventional reinforcing elements in end zones. The following conclusions are drawn

- The load-carrying capacity of the specimens with the GFRP rebars was 14.0% higher than that of those with the steel rebars and meshes, although the reinforcement ratio of the meshed blocks was approximately one-tenth the ratio of the others. The capacity of the steel-reinforced specimens was susceptible to the number of rebars and mesh layers, which was not the case for the GFRP-reinforced specimens.
- The post-peak load drop of the steel- and GFRP-reinforced specimens was comparable because axial stresses were distributed in the unreinforced concrete zone, whereas the drop was precipitous for the specimens with the meshes that intersected the concrete in orthogonal directions. A combination of these disparate reinforcing elements may be used

in practice to complement the weaknesses of each, improving capacity and post-peak failure performance.

- The local tension underneath the axial compression caused the concrete to split. The location of cracking and its pattern changed with the number of embedded rebars due to alterations in the load path of stress trajectories. This tendency was not recognized in the specimens with the meshes. The low modulus GFRP rebars permitted extended crack openings, as opposed to the narrow openings associated with the meshes featuring multilateral layouts in the concrete block.
- Away from the loaded end, the isostatic lines of compression progressively ascended and stabilized, resulting in horizontal bursting forces that cracked the blocks. When the external load was greater than the cracking load ($P > P_{cr}$), the bursting force substantially increased, and at least two rebars should be placed to effectively manage internal stresses.
- The loaded area ratio (a/h) and concrete strength (f'_c) of the specimens dominated the cracking load, while the contribution of other geometric properties such as the thickness ratio (t/h) was negligible. The importance of grid size in the meshes was noteworthy for stress development.
- The empirical stress limit of 20 ksi stated in the AASHTO LRFD Bridge Design Specifications (AASHTO 2020) was acceptable for the discrete rebars in the end zone. Further research is necessary on the continuous meshes to establish new design limits.

I.7. References

AASHTO. 2020. AASHTO LRFD bridge design specifications (9th edition), American Association of State Highway and Transportation Officials, Washington, D.C.

ACI. 2019. Building code requirements for structural concrete and commentary (ACI 318-19), American Concrete Institute, Farmington Hills, MI.

ACI. 2021. Strut-and-tie method guidelines for ACI 318-19 (ACI PRC-445.2-21), American Concrete Institute, Farmington Hills, MI.

ACI. 2022. Building code requirements for structural concrete reinforced with glass fiber-reinforced polymer (GFRP) bars- code and commentary (ACI 440.11-22), American Concrete Institute, Farmington Hills, MI.

ASTM. 2021. Standard test method for compressive strength of cylindrical concrete specimens (ASTM C39-21), ASTM International, West Conshohocken, PA.

Burdet, O. 1990. Analysis and design of anchorage zones for posttensioned concrete bridges, Ph.D. Dissertation, University of Texas at Austin, Austin, TX.

Breen, J. E., Burdet, O., Roberts, C., Sanders, D., and Wollmann, G. 1994. Anchorage zone reinforcement for post-tensioned concrete girders, NCHRP Report 356, Transportation Research Board, Washington, D.C.

Chiriatti, L., Mercado-Mendoza, H., Apedo, K.L., Fond, C., and Feugeas, F. 2019. A study of bond between steel rebar and concrete under a friction-based approach, Cement and Concrete Research, 120, 132-141.

Cui, M., Nie, X., Fan, J., Li, S., Liufu, J., and Huang, Z. 2019. Experimental study on the shear performance of RC beams reinforced with welded reinforcement grids, Construction and Building Materials, 203, 377-391.

Drar, A.A.M. and Matsumoto, T. 2016. Fatigue analysis of RC slabs reinforced with plain bars based on the bridging stress degradation concept, Journal of Advanced Concrete Technology, 14, 21-34.

El-Metwally, S. and Chen, W.F. 2017. Structural concrete: strut-and-tie models for unified design, CRC Press, Boca Raton, FL.

Esmaeili, Y., Eslami, A., Newhook, J., and Benmokrane, B.2020. Performance of GFRP-reinforced concrete beams subjected to high-sustained load and natural aging for 10 Years, Journal of Composites for Construction, 24(5), 04020054.

He, Z.-Q. and Liu, Z. 2011. Investigation of bursting forces in anchorage zones: compression-dispersion models and unified design equation, Journal of Bridge Engineering, 16(6), 820-827.

Hiremath, G., Itani, R., and Vasishth, U. 1989. Test of continuous prestressed concrete girders without end blocks, Transportation Research Record, 1223, 73-83.

Hou, D.-W., Zhao, J.-L., Shen, S.-L., and Chen, J. 2017. Investigation and improvement of strut-and-tie model for design of end anchorage zone in post-tensioned concrete structure, Construction and Building Materials, 136, 482-494.

Geng, X., Zhou, W., and Yan, J. 2019. Reinforcement of orthogonal ties in steel-fiber-reinforced reactive powder concrete anchorage zone, Advances in Structural Engineering, 22(10), 2311-2321.

Guyon, Y. 1955. Prestressed concrete, Contractors Record, London, UK.

Mukhtar, F. and Deifalla, A. 2023. Shear strength of FRP reinforced deep concrete beams without stirrups: test database and a critical shear crack-based model, Composite Structures, 307, 116636.

Nawy, E.G. 2009. Prestressed concrete (5^{th} edition), Prentice Hall, Upper Saddle River, NJ.

Okumus, P. and Oliva, M.G. 2013. Evaluation of crack control methods for end zone cracking in prestressed concrete bridge girders, PCI Journal, 58(2), 91-105.

Oluokun, F.A. 1991. Prediction of concrete tensile strength from its compressive strength, ACI Materials Journal, 88(3), 302-309.

Sahoo, D.K., Singh, B., and Bhargava, P. 2009. Investigation of dispersion of compression in bottle-shaped struts, ACI Structural Journal, 106(2), 178-186.

Sanders, D.H. and Breen, J.E. 1997. Post-tensioned anchorage zones with single straight concentric anchorages, ACI Structural Journal, 94(2), 146-158.

Sawpan, M.A. 2016. Effects of alkaline conditioning and temperature on the properties of glass fiber polymer composite rebar, Polymer Composites, 37(11), 3181-3190.

Srinivasan, S.S., Rung, M., and Ferron, R.D. 2020. Factors affecting loss in durability in prestressed-concrete girders with microcracking, Journal of Bridge Engineering, 25(9), 04020068.

Steensels, R., Vandoren, B., Vandewalle, L., and Degee, H. 2019. Evaluation of end-zone detailing of pre-tensioned concrete girders, Engineering Structures, 187, 372-383.

Tuan, C.Y., Yehia, S.A., Jongpitaksseel, N., and Tadros, M.K. 2004. End zone reinforcement for pretensioned concrete girders, PCI Journal, 49(3), 68-82.

Ugural, A. C. and Fenster, S. K. 1995. Advanced strength and applied elasticity (3rd edition), Prentice-Hall, Hoboken, NJ.

Yao, G., Xiong, X., and Ge, Y. 2021. Cracking behavior of full-scale pre-tensioned prestressed concrete double-Tee members with steel-wire meshes, Journal of Building Engineering, 44, 102658.

Zhou, L., Liu, Z., and He, Z. 2017. Elastic-to-plastic strut-and-tie model for concentric anchorage zones, Journal of Bridge Engineering, 22(10), 04017070.

Part II: End-Zone Reinforcing Schemes for Prestressed Concrete Bulb-Tee Girders

II.1. Introduction

End-zone cracking, which occurs in the horizontal and diagonal directions when strands are detensioned, is commonplace in prestressed concrete girders (Arab et al. 2014; Yapar et al. 2015). The size of end zones is traditionally defined as per St. Venant's principle, meaning that the length of an end zone may be assumed to be the vertical dimension of the member (AASHTO 2020). The distribution of stresses in end zones is complex due to the simultaneous interaction of multiple prestressing strands and ordinary rebars under transferred forces. Premature end-zone cracking can cause problems in both functionality and durability: detrimental chemicals may penetrate and accelerate the deterioration of prestressed concrete girders (Salas et al. 2008), while dimensional changes in partially released strands can reduce the desired level of prestressing forces (Abdel-Jaber and Glisic 2019). Another issue is that, once initiated, cracks can evolve over time and shorten the service life of girders (Yapar et al. 2015). For these reasons, end zones are considered an important component of pretensioned girders and transportation agencies are eager to find effective solutions that can alleviate the repercussions of unintended cracking.

The arrangement of reinforcing bars in end zones is crucial for crack control, force transfer, and stress mitigation (Ross et al. 2014). It is important to state that the purpose of crack control is to limit a crack width within tolerable limits, rather than to prevent cracking in girder concrete. Practice manuals and codes stipulate allowable crack widths of 0.007 in. to 0.012 in., depending upon operational environments (ACI 2001; PCI 2006). Vertical reinforcing bars are typically installed to counteract the stresses resulting from prestressing forces. Splitting forces across girder sections are often approximated as a fraction of the total prestressing force (Tadros et al. 2010) and rebars are located within a distance of $h/4$ from the girder end, where h is the depth of the girder (AASHTO 2020). Several reinforcing strategies have been attempted to address concerns related to the cracking of end zones. Ross et al. (2014) established a relationship between the number of vertical rebars and the progression of cracks in the end zone of prestressed concrete members. Four to eight rebars were placed and web-splitting cracks were monitored. Experimental findings signified that the articles of the American Association of State Highway and Transportation Officials (AASHTO) Load and Resistance Factor Design (LRFD) Bridge Design Specifications (AASHTO 2020) were inadequate and confirmed that rebar

diameters were instrumental in controlling the cracks. Steinberg and Semendary (2017) developed a computer model to predict the stress of vertical rebars embedded in the end zones of prestressed bulb-tee girders. Instead of the 6 in. reinforcement spacings specified in regional specifications, narrower spacings of 3 in. were employed with twice as many rebars. The substitute placement of the rebars lowered principal tensile strains, whereas the intricate interactions between the rebars and concrete cracking were not explained. Yao et al. (2021) tested double-tee beams reinforced with two layers of steel meshes (0.24 in. in diameter). The deployed meshes lessened strains on other rebars near midspan and the distributed reinforcement appropriately transmitted tensile stresses within the highly loaded area. Xiong et al. (2023) extended the foregoing test and assessed the performance of steel meshes in the shear span of double-tee beams, encompassing the end zones. The growth of diagonal tension cracks was logged and concrete strains were gauged. The positioning of the meshes was beneficial for elevating the capacity of the beams.

Despite significant efforts, there is still an insufficient understanding of end zone behavior and federally accepted reinforcing details and arrangements are not yet available. This study explores crack control in end zones with varying layouts of reinforcing bars through three-dimensional finite element modeling. A full-scale benchmark girder is adapted from the standard sheets of the Colorado Department of Transportation and refined stress analysis is conducted to evaluate the adequacy of the end-zone reinforcement. Parametric studies broaden the scope of the computational models by accounting for a diverse array of variables, namely, C-bar spacing and size (No. 5 to No. 7 spaced 6 in. to 17.7 in.), girder height (54 in. to 90 in.), and welded wire fabric.

II.2. Research Significance

To advance the state of the art in prestressed concrete girders, comprehensive insights are necessary to propose effective reinforcing techniques for end zones. Empirically developed design provisions dominate current practice (AASHTO 2020), which were initially proposed in the 1950s and 1960s (Guyon 1955; Marshall and Mattock 1962). Furthermore, most specifications do not provide sufficient guidelines on rebar configurations (PCI 2017; AASHTO 2020); as a result, practitioners rely heavily upon past experience without questioning its appropriateness. Discrepancies in published specifications are noteworthy as well; for example,

stress limits for end-zone rebars are specified as 20 ksi and 30 ksi in the AASHTO LRFD Bridge Design Specifications (AASHTO 2020) and the PCI Design Handbook (PCI 2017), respectively. As such, proper guidance is essential along with scientific investigations into the behavior of end zones with various reinforcing schemes. The research seeks to suggest practice recommendations to resolve these identified challenges.

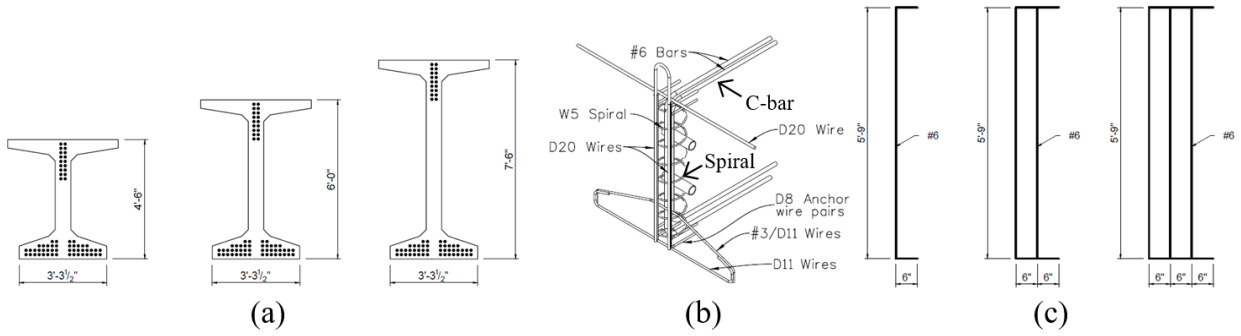

Fig. II.1. Benchmark girders: (a) dimension; (b) default reinforcement in end zone; (c) C-bar configuration

II.3. Benchmark Girders

The CBT72 prestressed concrete girder from the Colorado Department of Transportation (CDOT) was selected as the default structure (Fig. II.1(a)) together with CBT54 and CBT90, which were used for parametric examinations (unless explicitly mentioned, technical outcomes in this report indicate those of CBT72). While all girders possessed the same flange width of b_f = 50 in. and a length of L = 120 ft, the CBT 72 girder had an overall depth of h = 6 ft and those of CBT54 and CBT90 were h = 4.5 ft and 7.5 ft, respectively (Table II.1). Pursuant to the CDOT Bridge Design Manual (CDOT 2022), the 28-day compressive concrete strength was f'_c = 8.5 ksi with a strength of f'_{ci} = 6.5 ksi at transfer. The elastic moduli of the concrete were estimated to be E_c = 5,400 ksi and E_{ci} = 4,700 ksi in accordance with the AASHTO LRFD Bridge Design Specifications (AASHTO 2020). The CBT72, CBT54, and CBT90 girders incorporated 64 steel strands for the sake of comparison, each with a diameter of ϕ_p = 0.6 in. and a cross-sectional area of A_p = 0.207 in.^{2}. The tensile strength and elastic modulus of the strands were f_{pu} = 270 ksi and E_p = 28,500 ksi. Grade 60 reinforcing bars, featuring a yield strength of f_y = 60 ksi and an elastic modulus of E_s = 29,000 ksi, were placed as instructed in the standard drawing of CDOT (Fig. II.1(b)). The centers of gravity of the concrete (CGC) and steel (CGS) in CBT 72 were 35.1 in.

and 5.7 in. from the girder bottom (Table II.1), respectively, and two harping points were adopted at 0.4L (PCI 2023). The primary reinforcement in the end zone of the girders was a pair of No. 6 bars (ϕ_s = 0.75 in. and A_s = 0.44 in.^{2}, each), called C-bars (Fig. II.1(b)), and the W5 spiral (diameter = 5 in.) at a pitch of 4 in. The major parameter of the present study was the number of C-bars, varying from one to three pairs (Fig. II.1(c): one to three C-bars hereafter). The tail length of the C-bar in Fig. II.1(b) is 27 in.; however, it was adjusted to 6 in. to allow multiple C-bars positioned at 6 in. spacings. This modification was not problematic, as the bars effectively resist vertical stresses from prestressing forces, and a preliminary study confirmed that the tail length of C-bars did not affect their resistance.

Table II.1. Properties of benchmark girders

Girder	h (in.)	h_w (in.)	A_g (in.^{2})	I_g (in.^{4})	CGC (in.)	CGS (in.)	W (lb/ft)
CBT54	54	30.875	908	378,473	26.40	5.66	971
CBT72	72	48.875	1,034	767,268	35.10	5.66	1,106
CBT90	90	66.875	1,160	1,323,390	43.87	5.66	1,240

h = total height; h_w = web height; A_g = gross cross-sectional area; I_g = gross moment of inertia; CGC = center of gravity of concrete from girder bottom; CGS = center of gravity of steel from girder bottom at midspan; W = self-weight

II.4. Finite Element Modeling

Described below is the development of finite element models. Emphasis is placed on the constitutive relationships of materials, the formulation of elements and boundary conditions, and the progression of damage in conjunction with experimental verification.

II.4.1. Constitutive Modeling

The stress-strain relationships of concrete in compression and tension (σ_c and σ_t in Figs. II.2(a) and (b), respectively) were established by (Hordijk 1992; *fib* 2010; Alfah et al. 2017)

$$\sigma_{c1} = E_0 \varepsilon_c \tag{II.1}$$

$$\sigma_{c2} = \frac{E_{ci}\dfrac{\varepsilon_c}{f_{cm}} - \left(\dfrac{\varepsilon_c}{\varepsilon_{cm}}\right)^2}{1 + \left(E_{ci}\dfrac{\varepsilon_{cm}}{f_{cm}} - 2\right)\dfrac{\varepsilon_c}{\varepsilon_{cm}}} f_{cm} \tag{II.2}$$

$$\sigma_{c3} = \left(\frac{2 + \gamma_c f_{cm} \varepsilon_{cm}}{2 f_c^{'}} - \gamma_c \varepsilon_c + \frac{\varepsilon_c^2 \gamma_c}{2 \varepsilon_{cm}} \right)^{-1} \tag{II.3}$$

$$\gamma_c = \frac{\pi^2 f_{cm} \varepsilon_{cm}}{2 \left[\frac{G_{ch}}{l_{eq}} - 0.5 f_{cm} \left(\varepsilon_{cm} \left(1 - \frac{\varepsilon_c^{pl}}{\varepsilon_c^{ch}} \right) + \frac{\varepsilon_c^{pl}}{\varepsilon_c^{ch}} \frac{f_{cm}}{E_0} \right) \right]^2} \tag{II.4}$$

$$\sigma_t = \left\{ \left[1 + \left(c_1 \frac{w}{w_c} \right)^3 \right] e^{-c_2 \frac{w}{w_c}} - \frac{w}{w_c} \left(1 + c_1^3 \right) e^{-c_2} \right\} f_{tm} \tag{II.5}$$

where σ_{c1} is the linear elastic segment up to $0.4f_{cm}$; σ_{c2} is the post-linear segment up to f_{cm}; σ_{c3} is the softening segment; f_{cm} is the characteristic compressive strength of the concrete ($f_{cm} = f'_c + 8$ in MPa); E_0 is the elastic modulus of the concrete ($E_0 = (0.8+0.2f_{cm}/88)E_{ci}$ in MPa); E_{ci} is the modulus of deformation ($E_{ci} = 10{,}000\ (f'_c)^{1/3}$ in MPa); ε_c is the concrete strain; ε_{cm} is the strain at f_{cm} ($\varepsilon_{cm} = 0.0022$); G_{ch} is the crushing energy per unit area (Kratzig and Polling 2004); l_{eq} is the characteristic length (Kratzig and Polling 2004); ε_c^{pl} and ε_c^{ch} are the characteristic strains; c_1 and c_2 are constants ($c_1 = 0.3$ and $c_2 = 6.93$); w is the crack width; w_c is the fracture crack opening ($w_c = 5.14(0.073f_{cm}^{0.18}/f_{tm})$ in MPa); and f_{tm} is the tensile strength of the concrete. The reinforcing bars showed bilinear behavior based on the aforementioned material properties. The relationship for prestressing steel strands was (Fig. II.2(c), PCI 2017)

$$f_p = E_p \varepsilon_p \qquad \text{for } \varepsilon_p \le 0.0086 \tag{II.6a}$$

$$f_p = f_{pu} - \frac{k_1}{\varepsilon_p - 0.007} \qquad \text{for } \varepsilon_s > 0.0086 \tag{II.6b}$$

where f_p and ε_p are the stress and strain of the strands, respectively; and k_1 is the constant ($k_1 =$ 0.28 and 0.04 for the metric and US customary units, respectively).

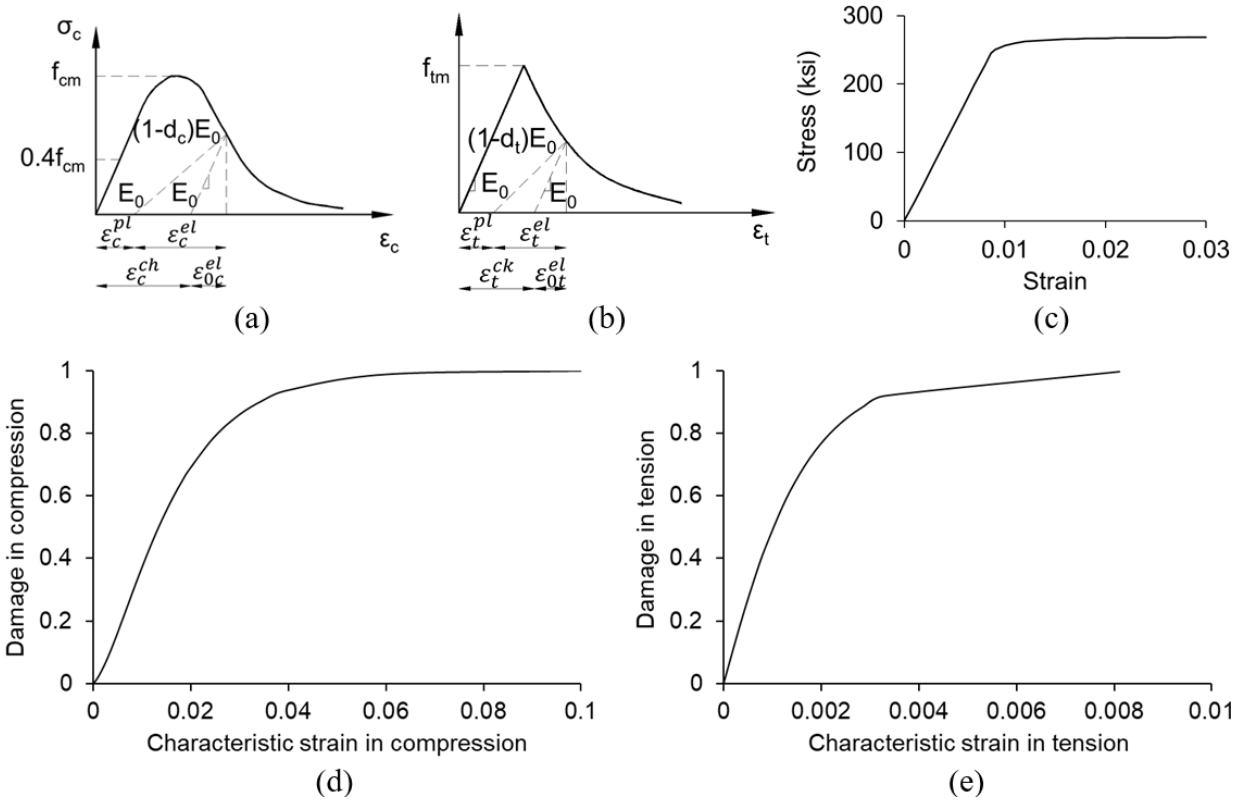

Fig. II.2. Constitutive relationship: (a) concrete in compression; (b) concrete in tension; (c) prestressing strands in tension; (d) damage in compression (D_c vs. ε_c^{ch}); (e) damage in tension (D_t vs. ε_t^{ck})

II.4.2. Model Formulation

The general-purpose finite element analysis package ABAQUS was employed to model the benchmark bridge girders. Three-dimensional solid elements (C3D8) simulated the concrete. The element comprised eight nodes and three translational degrees of freedom per node. The rebars, prestressing strands, and spirals were modeled by two-node truss elements (T3D2) having the same translational degrees of freedom as the solid elements. The progression of damage in the concrete was represented by isotropic elasticity alongside tensile plasticity (ABAQUS 2016). This algorithm is useful to accommodate crack opening after concrete cracking. The damage plasticity model entails property degradation, reducing the elastic modulus of the concrete

$$E_D = (1-D)E_0 \tag{II.7}$$

where E_D is the modulus of the damaged concrete and D is the damage index (D_c and D_t for compression and tension, respectively, Alfarah et al. 2017)

$$D_c = 1 - \frac{1}{(2+a_c)}\left[2(1+a_c)e^{-b_c\varepsilon_c^{ch}} - a_c e^{-2b_c\varepsilon_c^{ch}}\right] \quad \text{(II.8)}$$

$$D_t = 1 - \frac{1}{(2+a_t)}\left[2(1+a_t)e^{-b_t\varepsilon_t^{ck}} - a_t e^{-2b_t\varepsilon_t^{ck}}\right] \quad \text{(II.9)}$$

$$a_c = 2(f_{cm}/f_{c0}) - 1 + 2\sqrt{(f_{cm}/f_{c0})^2 - (f_{cm}/f_{c0})} \quad \text{(II.10)}$$

$$a_t = 2(f_{cm}/f_{t0}) - 1 + 2\sqrt{(f_{tm}/f_{t0})^2 - (f_{tm}/f_{t0})} \quad \text{(II.11)}$$

$$b_c = \frac{f_{c0}l_{eq}}{G_{ch}}\left(1 + \frac{a_c}{2}\right) \quad \text{(II.12)}$$

$$b_t = \frac{f_{t0}l_{eq}}{G_F}\left(1 + \frac{a_t}{2}\right) \quad \text{(II.13)}$$

where f_{c0} and f_{t0} are the stresses in compression and tension at $\varepsilon_c^{ch} = 0$ and $\varepsilon_t^{ck} = 0$, respectively; and G_F is the fracture energy ($G_F = 0.073 f_{cm}^{0.18}$ in MPa). Figures II.2(d) and (e) illustrate the evolution of damage in compression and tension with respect to the characteristic strains of ε_c^{ch} and ε_t^{ck}, respectively. For the connection between the concrete and rebars, full composite action was established through the concept of embedded nodes, sharing the same degrees of freedom (Garg and Abolmaali 2009). The bond-slip behavior of the prestressing strands was derived from the Model Code 2010 (*fib* 2010) with a 50% diminution in the bond stress to compensate for the surface condition of the strands (*fib* 2009). The strands were prestressed by means of a temperature adjustment technique frequently employed in the modeling community (Ren et al. 2015).

$$P_p = -\alpha_T E_P A_P \Delta T \quad \text{(II.14)}$$

where P_p is the prestressing force; α_T is the coefficient of thermal expansion ($\alpha_T = 6.7\times10^{-6}/^{o}F$); and ΔT is the temperature difference. Given symmetric geometries, a quarter of each girder was modeled with a length of 13 ft to sufficiently cover the transfer length of the strands (to be revisited). According to a sensitivity analysis, an appropriate mesh size was found to be 1 in. The constructed model was solved using the explicit central-difference time integration rule (Boulbes 2019) and, to efficiently solve the nonlinear problem, the time-step increment was smaller than the stability limit, which was characterized by the length of the elements (ABAQUS 2016).

II.4.3. Validation

The modeling approaches were validated against an experimental program (O'Callaghan and Bayrak 2008). An I-shape girder (Tx28-II) was taken (Fig. II.3(a)) with a depth of h = 28 in. and a cross-sectional area of A_g = 585 in.^{2}. The girder was pretensioned using 36 seven-wire prestressing strands (0.6 in. in diameter) and reinforced by steel bars (0.75 in. in diameter). For end zones, a set of vertical rebars (0.75 in. in diameter) was placed at spacings of 3 in. to 4 in. The strength of the concrete was f'_{ci} = 6,500 psi at release, the yield strength of the rebars was f_y = 75 ksi, and the tensile strength of the strands was f_{pu} = 285 ksi. The initial level of prestressing was $0.80f_{pu}$, which decreased to $0.72f_{pu}$ after losses. When the prestressing forces were transferred, strain readings were recorded from the strands and end-zone rebars at three locations (14.5 in., 17.5 in., and 20.5 in. from the bottom of the girder). The formulated finite element model is visible in Fig. II.3(b). As shown in Fig. II.3(c), numerical damage near the end zone ($D_t \geq 0.4$) aligned with experimental cracks. Likewise, the measured stresses matched the predicted values (Figs. II.3(d) and (e)).

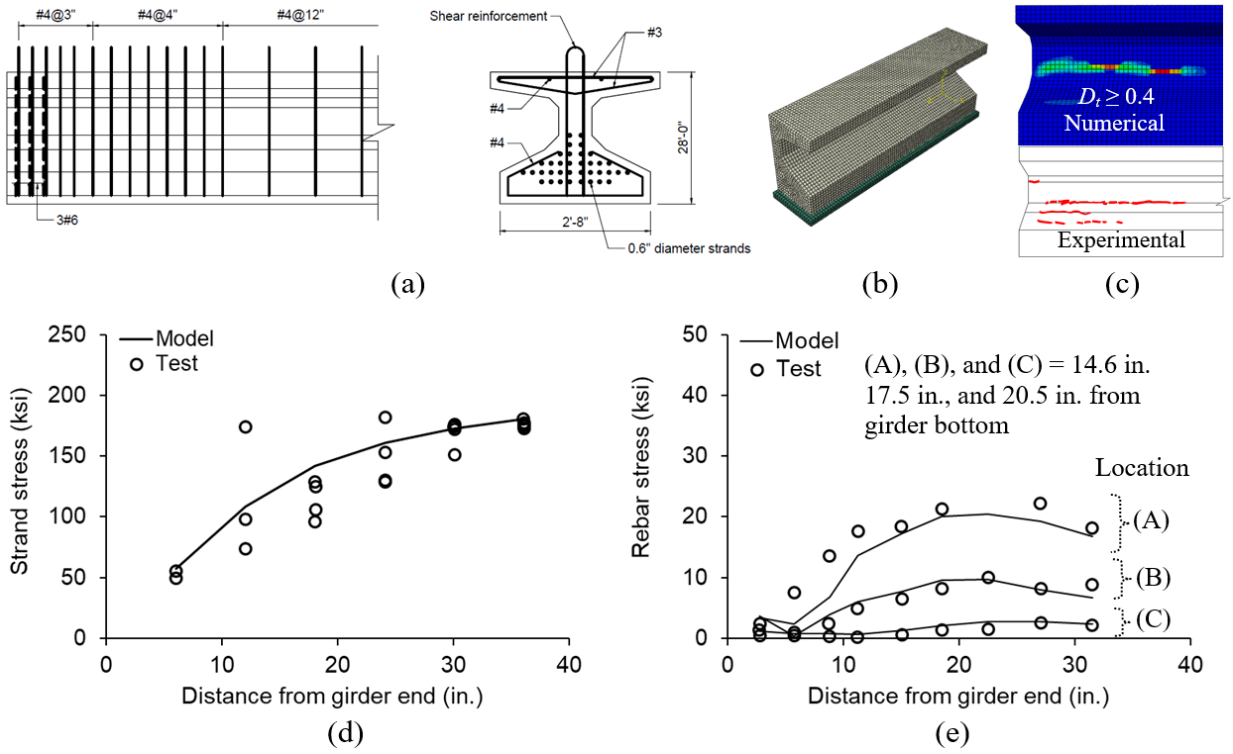

Fig. II.3. Model validation: (a) experimental girder (Tx28-II); (b) developed model; (c) damage vs. crack patterns; (d) strand stress; (e) vertical reinforcement stress

II.5. Results and Discussion

This section commences with an overview of simulation results concerning the behavior of end zones, followed by quantified information on strain development, cracking, damage, and splitting forces.

II.5.1. Contextual Overview

A cutaway view of the CBT72 girder model with three C-bars is depicted in Fig. II.4(a). The formulation of the computational model benefited from symmetric boundary conditions, as elaborated earlier, and prestressing strands and rebars were adequately positioned in compliance with the CDOT Bridge Design Manual (CDOT 2022). Figure II.4(b) illustrates the damage contours of the girder with zero and three C-bars. The presence of the C-bars lowered the severely damaged regions (D = 0.89), particularly along the harped strands, and decreased damage near the bottom of the web in an analogous manner. Regarding the maximum principal strains of the girders, appreciable reductions were noticed by adding the C-bars (Fig. II.4(c)). Given that the principal strains focus on normal strains with zero shear strains (Ugural and

Fenster 1995), the diminished maximum strains are an indication of controlled crack openings (to be discussed in a later section). The maximum axial stress of the C-bars spanned from 17.7 ksi to 18.8 ksi, which was around 30% of the yield stress (Fig. II.4(d)). The pattern of the maximum axial stress in the circumferential spirals was alike between 45.7% and 51.4% of the yield stress (Fig. II.4(e)). These facts imply that overstressing of the end-zone reinforcements was not of concern.

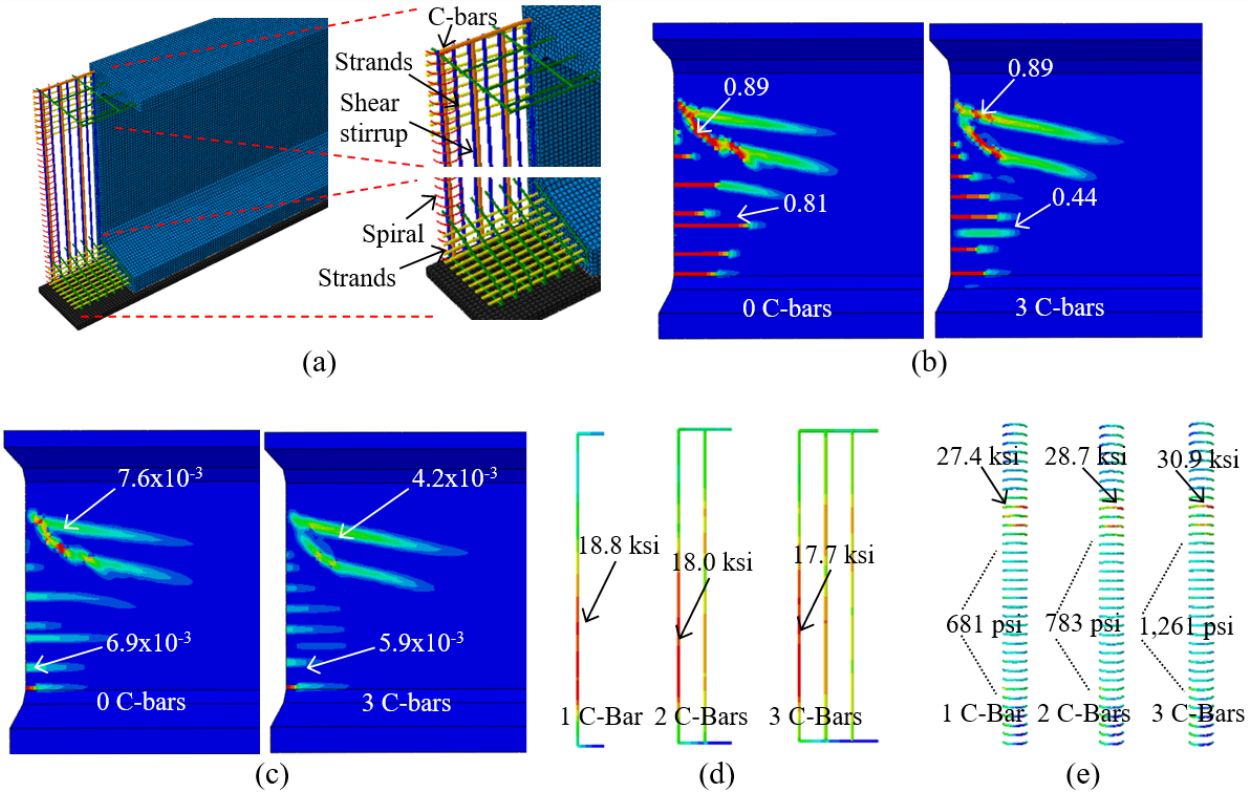

Fig. II.4. Girder model and contextual overview: (a) mesh formulation (cutaway view); (b) damage index; (c) maximum principal strain; (d) axial stress of C-bars; (e) axial stress of spirals

II.5.2. End-Zone Assessment

Figure II.5(a) exhibits the development of strand stress along the girder span, which was unaffected by the number of C-bars. The slope of the linearly ascending stress deviated at f_p/f_{pu} = 0.45 and the rate of increase stabilized after the normalized distance of 0.60, in which the longitudinal distance was divided by the girder height. The empirical transfer length of $60d_b$ specified in the AASHTO LRFD Bridge Design Specifications (AASHTO 2020) was reasonably acceptable: the $60d_b$ stress differed from the converged stress by 5.2%. Also shown in Fig. II.5(a)

is the stress level at the end-zone location of $h/4$ as defined by the AASHTO LRFD Bridge Design Specifications (AASHTO 2020). The strand stress was not fully developed at $h/4$ (f_p/f_{pu} = 0.53), suggesting that higher prestressing forces applied outside the zone might influence the behavior of the end zones. To further examine the ramifications of prestressing forces, the gradient of the maximum principal stresses was plotted near the end of the girder (Fig. II.5(b)). The $h/4$ limit coincided with the intensely stressed region close to the lower flange, where the straight strands were tensioned. Contrarily, the stresses adjacent to the upper portion of the web containing the inclined strands extended over $3h/4$. This observation underscores the potential inadequacy of the current limit mandated by the AASHTO LRFD Bridge Design Specifications (AASHTO 2020), supported by arguments from other researchers (Tadros et al. 2010; Ronanki et al. 2017). The variation of the maximum principal stresses at $0.2h$ and $0.7h$ from the girder bottom is compiled in Fig. II.5(c). The stresses continued to develop in excess of the $h/4$ limit with no dependence on the number of C-bars; however, a decline was discernible past the $3h/4$ limit (Fig. II.5(d)). Accordingly, the $3h/4$ limit is recommended for designating end zones where the C-bars are located.

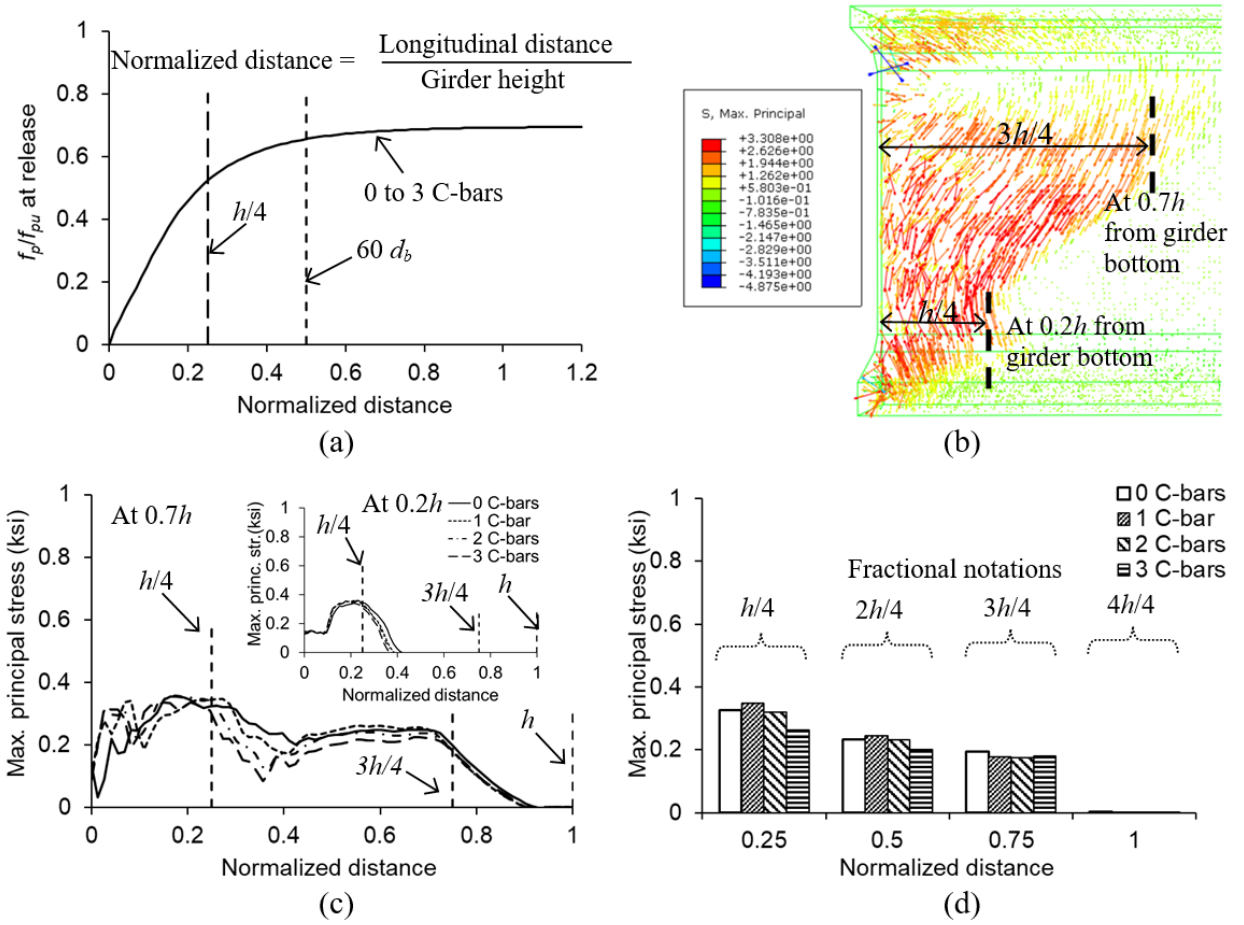

Fig. II.5. Assessment of end zone: (a) transfer length of strands along span; (b) maximum principal stress without C-bars (units in MPa; 1 MPa = 145 psi); (c) variation of maximum principal stress along span; (d) comparison of maximum principal stress at 0.7*h* along span

II.5.3. Reinforcement Response

The strains of the C-bars are graphed in Figs. II.6(a) to (c). When one bar was situated, the maximum tensile strain was 652×10^{-6} in proximity to the junction between the web and lower flange (Fig. II.6(a)). The strains dwindled as the distance from the girder bottom became greater, since more strands were tensioned in the lower flange than in the web. The moment caused by the eccentricities of the harped strands induced local compression in the C-bar. With the setting of two C-bars (Fig. II.6(b)), the maximum strain in the first bar decreased by 4.3% relative to the one-bar case and the peak strain in the second bar was 66.5% of that in the first bar. The foregoing local compression effect was apparent in the second bar at 39.4 in. from the bottom of the girder, where a strain drop was evident. The installation of three C-bars reduced the maximum strain of the first bar by 6.0% compared with the scenario of a single bar (Fig. II.6(c)).

Although the strains in the third bar were generally below the magnitude of those in the second bar, their responses were virtually identical beyond 49.2 in. from the girder bottom possibly owing to the redistribution of prestressing forces beneath the upper flange.

The profile of axial strains in the spirals around the circumferential direction is provided in Figs. II.6(d) to (f). Whereas the number of C-bars had little impact, the location of strain collection was remarkable. Among multiple spikes, the maximum strain on the outer side (toward the girder end) was detected in the vicinity of the upper web within which the slanted prestressing forces were transferred (Fig. II.6(d)). A comparable trend was recorded across the middle of the spirals (Fig. II.6(e)), except for the separate peak strains that were shared by the front and rear portions of the spirals. The peak strains on the inner side (away from the girder end) emerged 13.8 in. from the girder bottom (Fig. II.6(f)), arising from stress concentrations just above the haunches of the lower flange. Other than these peak locations, the spiral strains were trivial.

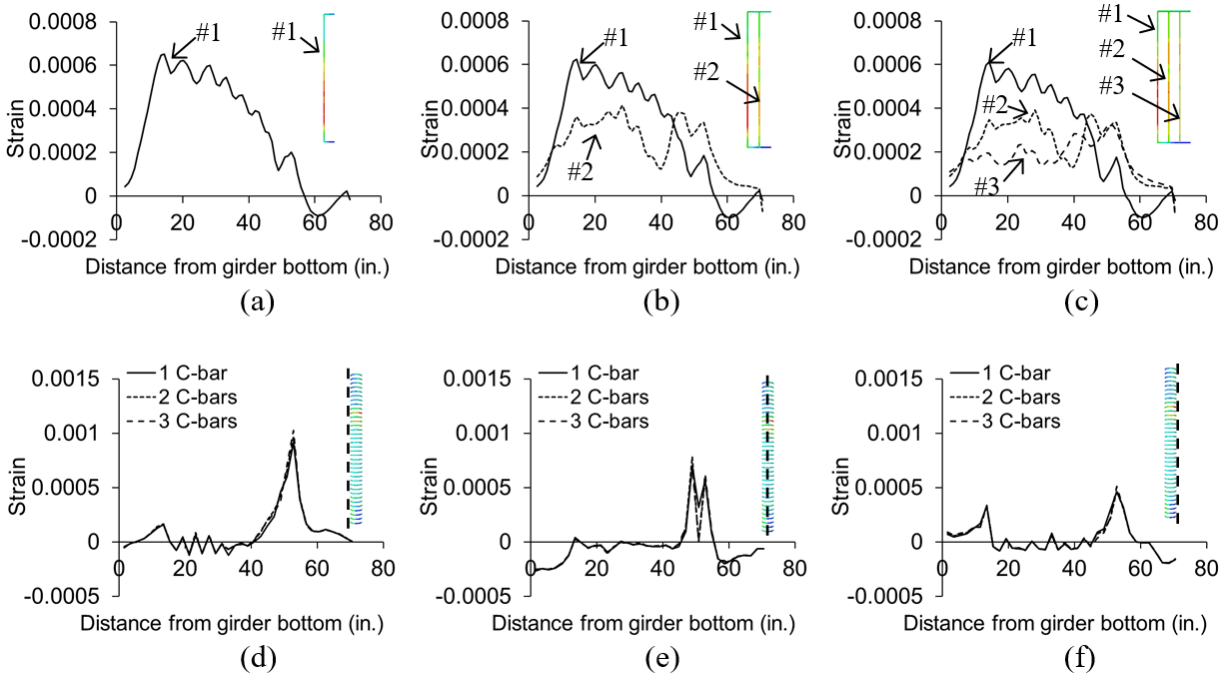

Fig. II.6. Response of end-zone reinforcement: (a) one C-bar: (b) two C-bars; (c) three C-bars; (d) spiral at outer location; (e) spiral at middle location; (f) spiral at inner location

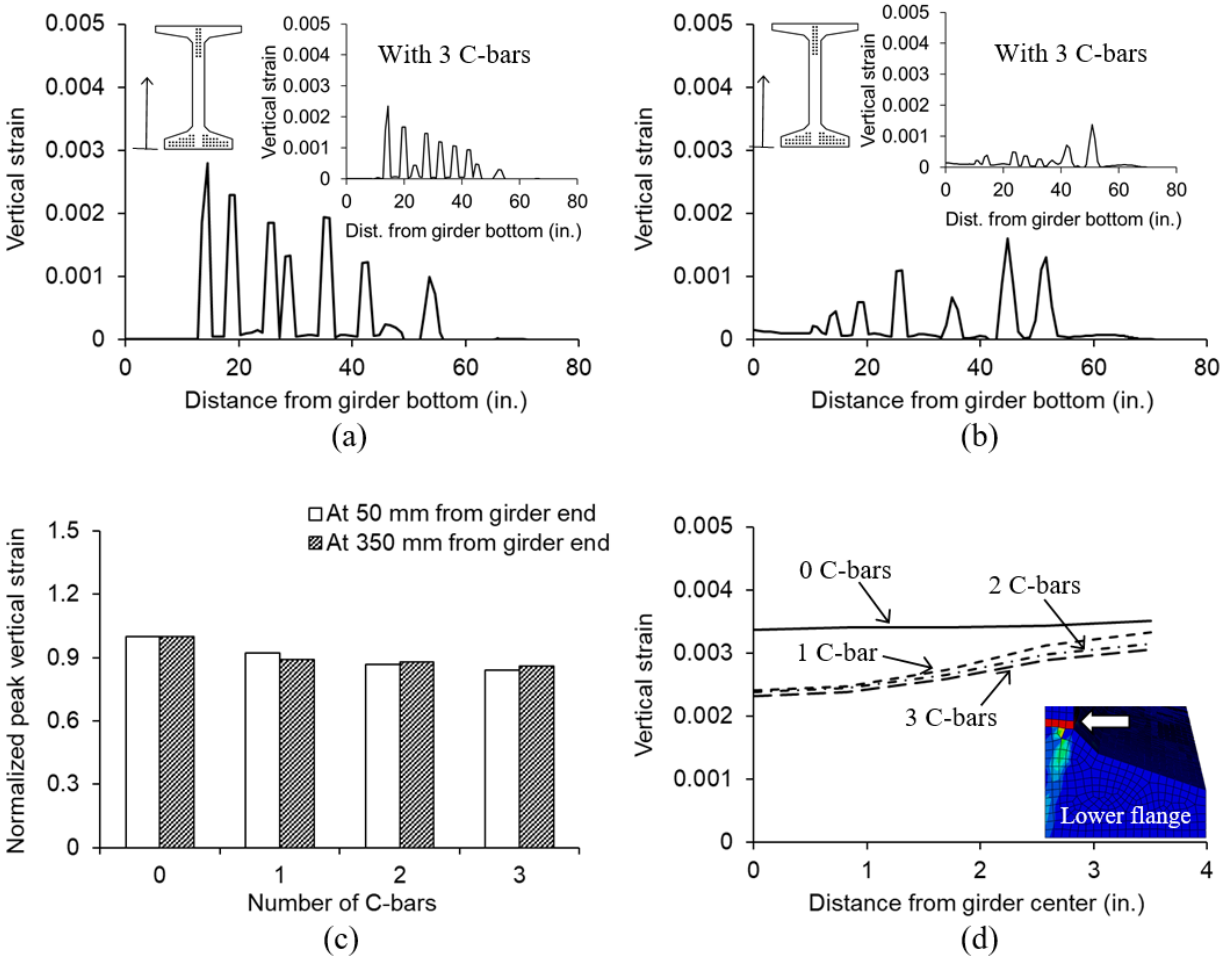

Fig. II.7. Development of concrete strain across girder depth: (a) vertical strain at 2 in. from girder end without C-bars; (b) vertical strain at 13.8 in. from girder end without C-bars; (c) normalized peak vertical strains; (d) vertical strain at junction between lower flange and web

II.5.4. Strain of Girder Concrete

Figure II.7 displays vertical strains in the concrete at selected locations across the depth of the girder. In the absence of C-bars, the strains at 2 in. and 13.8 in. from the girder end fluctuated periodically with maximum values of 0.0028 and 0.0016, respectively (Figs. II.7(a) and (b)). The effectiveness of the C-bars is reflected in the insets of Figs. II.7(a) and (b). The maximum strains of the girder with C-bars were normalized against those of the girder without C-bars for comparison and are charted in Fig. II.7(c). Discernible responses were noted with and without the C-bars, leading to a decrease of up to 15.9% at 2 in. and 13.8% at 13.8 in. The inclusion of the C-bars contributed to moderating the strains at the joint between the lower flange and the web (Fig. II.7(d), inset). The strain differences with one to three C-bars were marginal at the

center of the girder (Fig. II.7(d)); however, the values diverged as the readings moved away from the center (the strains discussed in Figs. II.7(a) to (c) were conservatively taken from the exterior elements, rather than from the center elements). In all circumstances, the setups involving two and three C-bars outperformed that with one C-bar.

Shown in Fig. II.8 are the vertical concrete strains along the length of the girder. The strains at 0.2*h* (13.8 in. from the bottom of the girder) gradually descended (Fig. II.8(a)): the strain with three C-bars was 12.7% less than the strain without C-bars at the girder end, while the disparity disappeared after 11.8 in. from the end. On the contrary, the strains at 0.7*h* (Fig. II.8(b), inset) altered markedly with the number of C-bars (Fig. II.8(b)). Figures II.8(c) and (d) reveal the implications of the C-bars in relation to the largest strains given in Figs. II.8(a) and (b), including the maximum principal strains that are directly associated with the cracking of concrete (Miura et al. 2020). The extent of strain reductions was modest at 0.2*h* (Fig. II.8(c)); in contrast, significant changes were recorded at 0.7*h* (Fig. II.8(d)) with the vertical and maximum principal strains varying by as much as 61.5% and 48.9%, respectively. It can thus be stated that the placement of the C-bars efficaciously controls the onset and progression of cracks stemming from the harped strands.

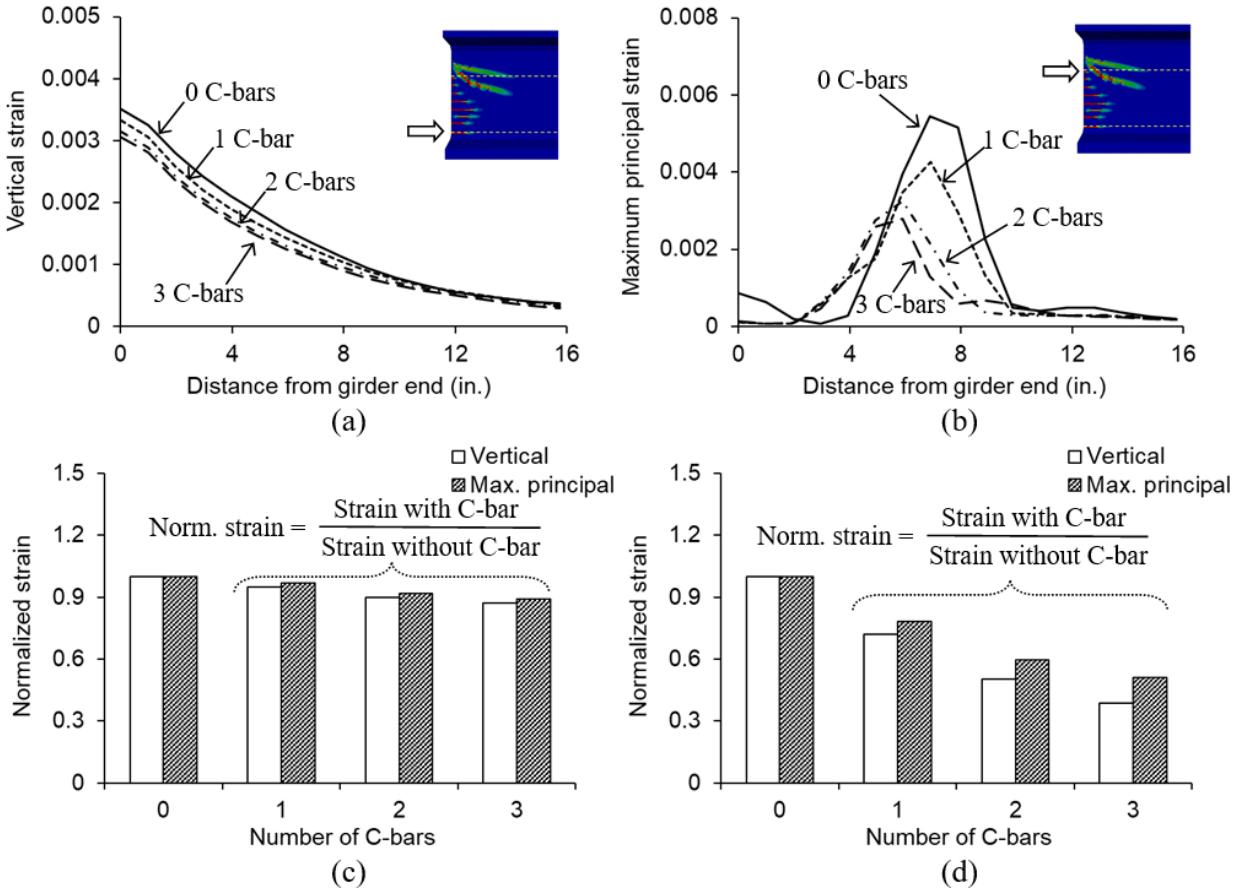

Fig. II.8. Development of concrete strain along girder length: (a) vertical strain at 0.2*h* from girder bottom; (b) maximum principal strain at 0.7*h* from girder bottom; (c) normalized strain at 0.2*h* from girder bottom; (d) normalized strain at 0.7*h* from girder bottom

II.5.5. Cracking of Girder Concrete

The crack width of the girder with and without the C-bars was determined using (CEN 2004)

$$w = s_{cr}\left(\varepsilon_s - \varepsilon_c\right) \tag{II.15}$$

where w is the probable short-term crack width of the concrete; s_{cr} is the crack spacing ($D_t \geq 0.4$ was assumed to be noticeable cracks, Fig. II.3(c)); ε_s is the steel strain (the strains of the shear stirrups were taken); and ε_c is the concrete strain between adjacent cracks. Additionally, the girder's long-term crack width was estimated by inferring the time-dependent strains of the concrete and rebars (ACI 2008; AASHTO 2020)

$$\varepsilon_c(t) = \varepsilon_c + \varepsilon_{cr} + \varepsilon_{sh} = (1+\psi_t)\varepsilon_c + \varepsilon_{sh} \quad \text{(II.16)}$$

$$\psi_t = 1.9 k_s k_{hc} k_f k_{td} t_i^{-0.118} \quad \text{(II.17)}$$

$$k_s = 1.45 - C_1(V/S) \geq 1.0 \quad \text{(II.18)}$$

$$k_{hc} = 1.56 - 0.008H \quad \text{(II.19)}$$

$$k_f = \frac{C_2}{C_3 + f_{ci}'} \quad \text{(II.20)}$$

$$k_{td} = \frac{t}{61 - C_4 f_{ci}' + t} \quad \text{(II.21)}$$

where ψ_t is the creep coefficient; C_1 to C_4 are calibration constants (C_1 = 0.0051 and 0.13, C_2 = 35 and 5, C_3 = 7 and 1, and C_4 = 0.58 and 4 for the metric and US customary units, respectively); H is the relative humidity (H = 55% was assumed for a typical city in the Midwest of the United States); V/S is the volume to surface ratio (V/S = 89 for the girder web); t is the maturity of the concrete (t = 36,500 days was assumed for 100 years); and t_i is the age of the concrete at the time of load application (t = 180 days was assumed for 6 months). For the long-term strain of the steel rebars, the short-term strain in Eq. II.15 was multiplied by the adjustment factor (increased concrete strain/steel modulus). The crack spacing (S_{cr}) was assumed invariant with time.

The crack positions that correlate with the spacing term in Eq. II.15 were identified (Fig. II.9(a)) and the strain values from the solved models were substituted into Eq. II.15. As seen in Fig. II.9(b), the C-bars played an important role in constraining the crack width of the girder concrete. Even if a crack width narrower than 0.02 in. is difficult to recognize visually (Leonhardt 1988), unfavorable substances can migrate through such cracks and impinge upon the durability of bridge girders (Wang et al. 2016). The alignment of the C-bars proved advantageous for the inclined strands in the web: the normalized short-term crack width at Position 1 declined by up to 29.5%; on the other hand, the width at Position 7 plummeted by more than 46.7% (Fig. II.9(c)). Figure II.9(d) appraises the average crack width of the girder (Positions 1 to 7) against the Deicing limit of ACI 224 (ACI 2001), contingent upon the number

of C-bars, which may necessitate an epoxy injection repair (PCI 2006). Unlike the short-term crack width with the C-bars, which did not exceed the limit of 0.007 in., the long-term crack width of the case with one C-bar reached the limit. Considering numerous uncertainties during the service life of prestressed concrete girders, two or three C-bars appear to be a better option for minimizing crack widths on site.

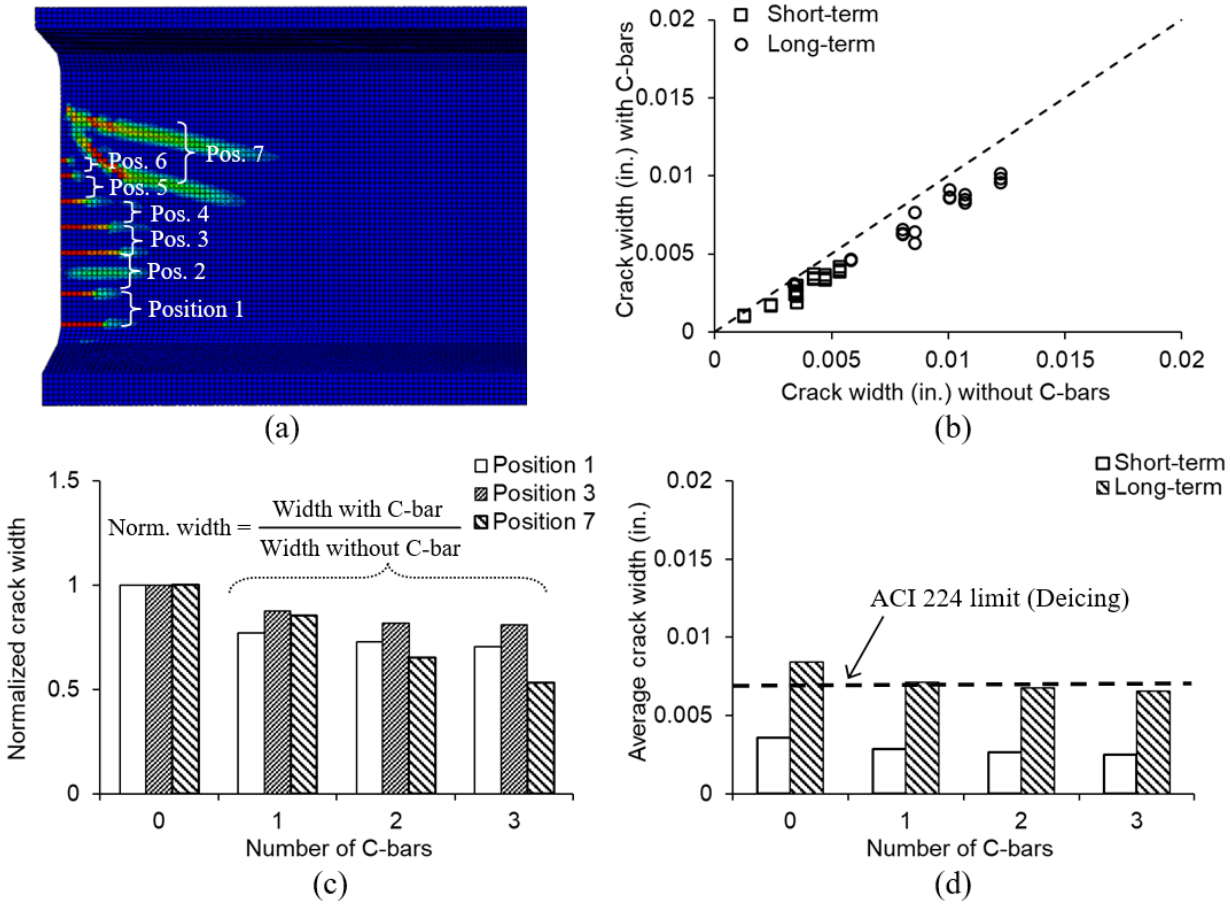

Fig. II.9. Crack width: (a) position; (b) comprehensive comparison; (c) normalized crack width for short-term prediction; (d) assessment

II.5.6. Damaged Area

The contours presented in Fig. II.4(b) were analyzed using graphics software to quantify the degree of damage in the end zones. The generated image files were imported into a Java-based program (Ferreira and Rashband 2012) and regions with $D_t \geq 0.4$ were classified as damaged areas for consistency. Figure II.10(a) visualizes the fraction of the damaged areas within the $h/4$ and $3h/4$ zones. When the girder was not reinforced with C-bars, 4.3% and 1.4% of the $h/4$ and

3*h*/4 zones were found to be damaged, respectively. These percentages consistently decreased with an increase in the number of C-bars. In light of the normalized fraction with and without the C-bars (Fig. II.10(b)), their presence restricted the damaged areas as low as 43.1%, corroborating the efficacy of the vertical reinforcement. As prescribed in ACI 302.1R-15 (ACI 2015), surface cracking up to 3% may be tolerable (no other guidance exists in any bridge specifications); hence, the 3*h*/4 end-zone area can be regarded as a suitable alternative to the conventional *h*/4 area.

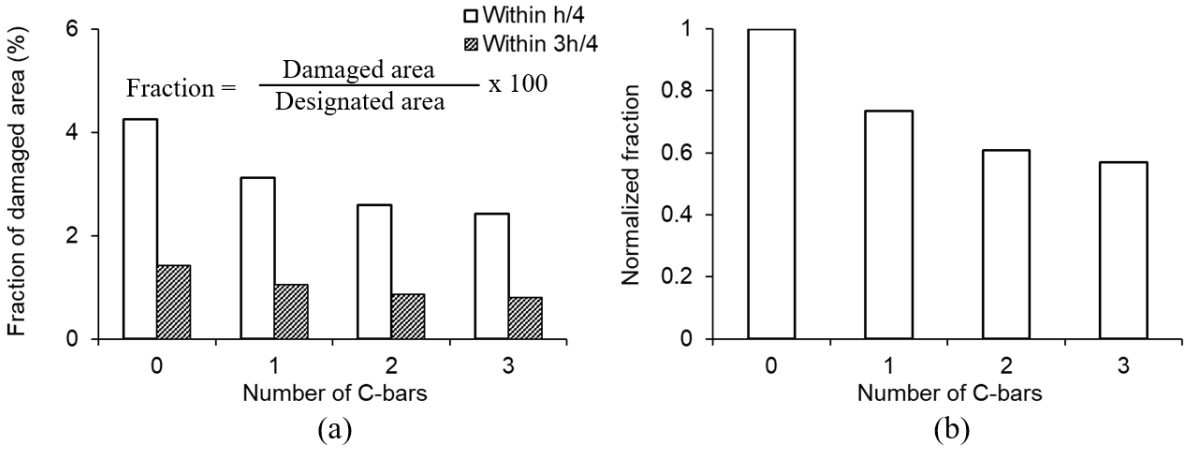

Fig. II.10. Damaged area: (a) fraction; (b) normalized fraction

II.5.7. Splitting Force

The maximum splitting force within the end zone (T_{sp}) may be calculated by Eq. II.22 (He and Liu 2011), similar to Eq. II.23 as stipulated in the AASHTO LRFD Bridge Design Specifications (AASHTO 2020)

$$T_{sp} = 0.22P(1+\gamma)^2\left[(1-\gamma)-\frac{a}{h}\right]+0.5P\left|\sin\theta\right|\left(1-\frac{a}{h}\right) \quad \text{(II.22)}$$

$$T_{burst} = 0.25\sum P\left(1-\frac{a}{h}\right)+0.5\left|\sum\left(P\sin\theta\right)\right| \quad \text{(II.23)}$$

where P is the prestressing force; γ is the eccentricity ratio ($\gamma = 2e/h$), in which e is the eccentricity of the strands; a is the width of the anchor plate; and θ is the angle of the

prestressing force in degrees. It is worth noting that Eq. II.23 was originally proposed for the bursting force of post-tensioned members with an anchor plate; however, by setting $a = 0$, it can be applied to pretensioned members. This claim is justified by the fact that the terms of splitting (T_{sp}) and bursting (T_{burst}) are technically synonymous, while their distinction in the AASHTO LRFD Bridge Design Specifications (AASHTO 2020) was made merely due to industry convention: the former refers to pretensioned members and the latter is for post-tensioned members (Mertz 2008).

The splitting force to prestressing force ratio of the individual strand layers ($T_{sp,i}/P_i$) is demonstrated in Fig. II.11(a). With the elevated eccentricities throughout the girder section (e/h), the ratio steadily waned; in addition, the splitting force component pertaining to the harped strands in the upper flange and web was larger than that of the straight strands in the lower flange. As far as strand angles are concerned (Fig. II.11(b)), it is obvious that the straight strands with $\theta = 0$ degrees did not contribute to the splitting forces (their eccentricities were influential). Therefore, to relieve the splitting forces in prestressed concrete girders, strand eccentricities and angles should be kept to a minimum. Figure II.11(c) evaluates the compatibility of the AASHTO expression with the refined formula. Within the previously covered boundaries of $0.2h$ and $0.7h$, Eqs. II.22 and II.23 produced the same splitting forces; however, substantial inconsistencies were observed in the flanges predominantly because strand eccentricities are not integrated into the AASHTO LRFD Bridge Design Specifications (AASHTO 2020). The average splitting force obtained from Eq. II.23 was greater than that from Eq. II.22 (Fig. II.11(d)), which may be acceptable for design; nonetheless, an improvement seems needed.

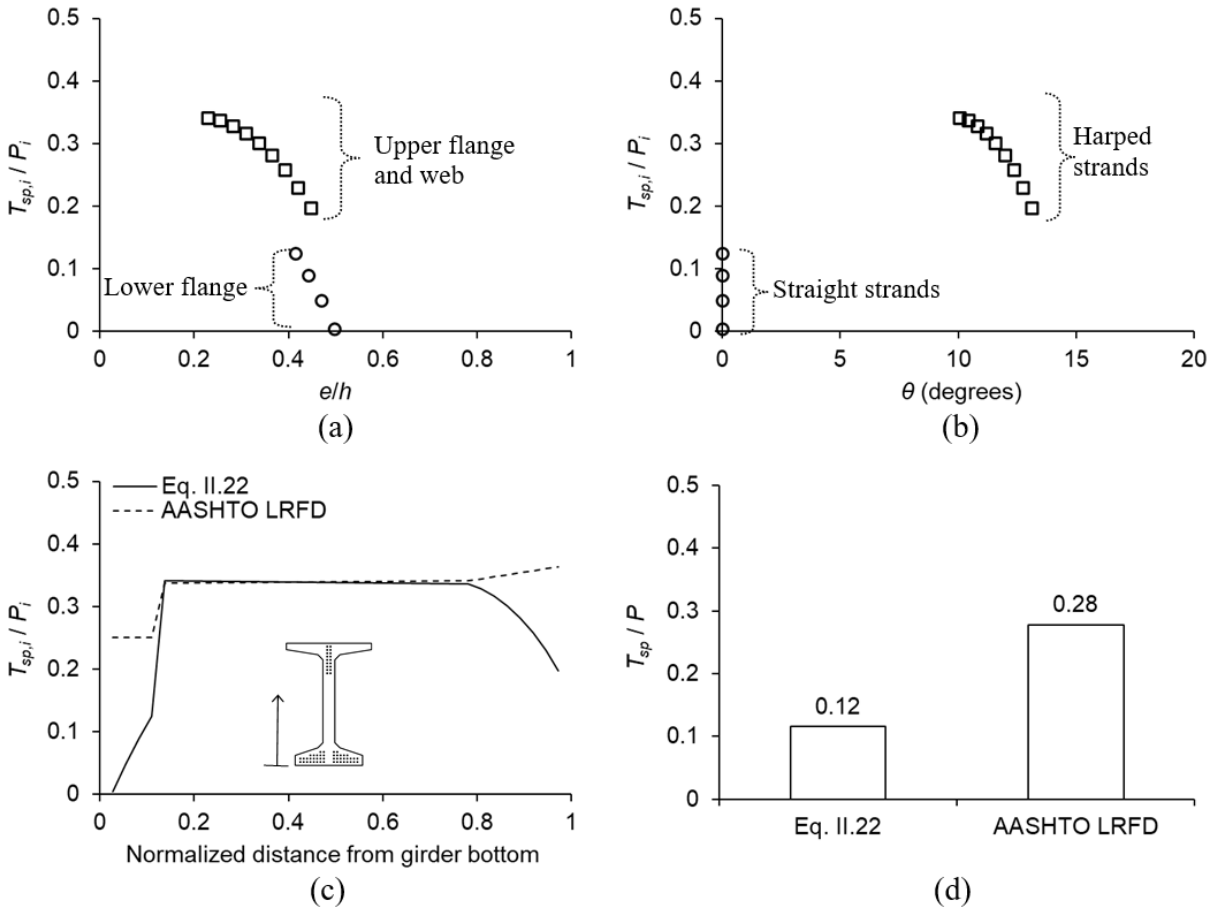

Fig. II.11. Development of splitting force within end zones: (a) eccentricity of i^{th} strands; (b) configuration of i^{th} strands; (c) assessment of specification equation; (d) ratio of total splitting force to total prestressing force

II.5.8. Parametric Studies

The effects of various C-bar properties, welded wire fabric, and girder depth were assessed. Unless otherwise stated, the geometric and material properties of CBT72 were retained as the default. Figure II.12(a) describes the maximum strain of No. 5, No. 6, and No. 7 C-bars (cross-sectional area = 0.31 in.^{2}, 0.44 in.^{2}, and 0.60 in.^{2}, respectively). The maximum strain ranged from 570×10^{-6} to 700×10^{-6}, with the difference between No. 5 and No. 6 (12.4%) being greater than that between No. 6 and No. 7 (7.0%). When the size of the C-bars increased, the vertical strains of concrete at the top of the lower flange lessened (Fig. II.12(b)) and again the difference between No. 6 and No.7 C-bars was smaller. These findings adduce that No. 5 C-bars may not be preferable in practice. The normalized vertical concrete strain at 0.7h and the average long-term crack width of the girder are rendered as a function of C-bar size in Figs. II.12(c) and (d),

respectively. The use of multiple C-bars, regardless of size, was beneficial in reducing the concrete strain and crack width. With regard to the spacing between C-bars, a narrower distance was more efficient in curbing concrete strains (Fig. II.12(e)); conversely, long-term crack widths were negligibly impacted (Fig. II.12(f)). The addition of welded wire fabric (W4.0×W4.0 with a steel area of 0.12 in.^{2}/ft) led to a considerable drop in the vertical strain of the concrete at 0.7*h* (Fig. II.13(a)), especially with two and three C-bars. The discrepancy in the long-term crack width with and without the welded wire fabric averaged 9.3% (Fig. II.13(b)). As the girder depth was raised from CBT54 to CBT90, the vertical concrete strains at the top of the lower flange escalated (Fig. II.13(c)) because of the enlarged eccentricities from the centroid of the girder. Moreover, the severity of damage near the lower end of the web in CBT90 was greater than in the other girders for the same cause (Fig. II.13(c), inset). The long-term crack width of the girders increased with depth (Fig. II.13(d)), reaffirming the necessity of multiple C-bars to systematically handle time-dependent durability matters.

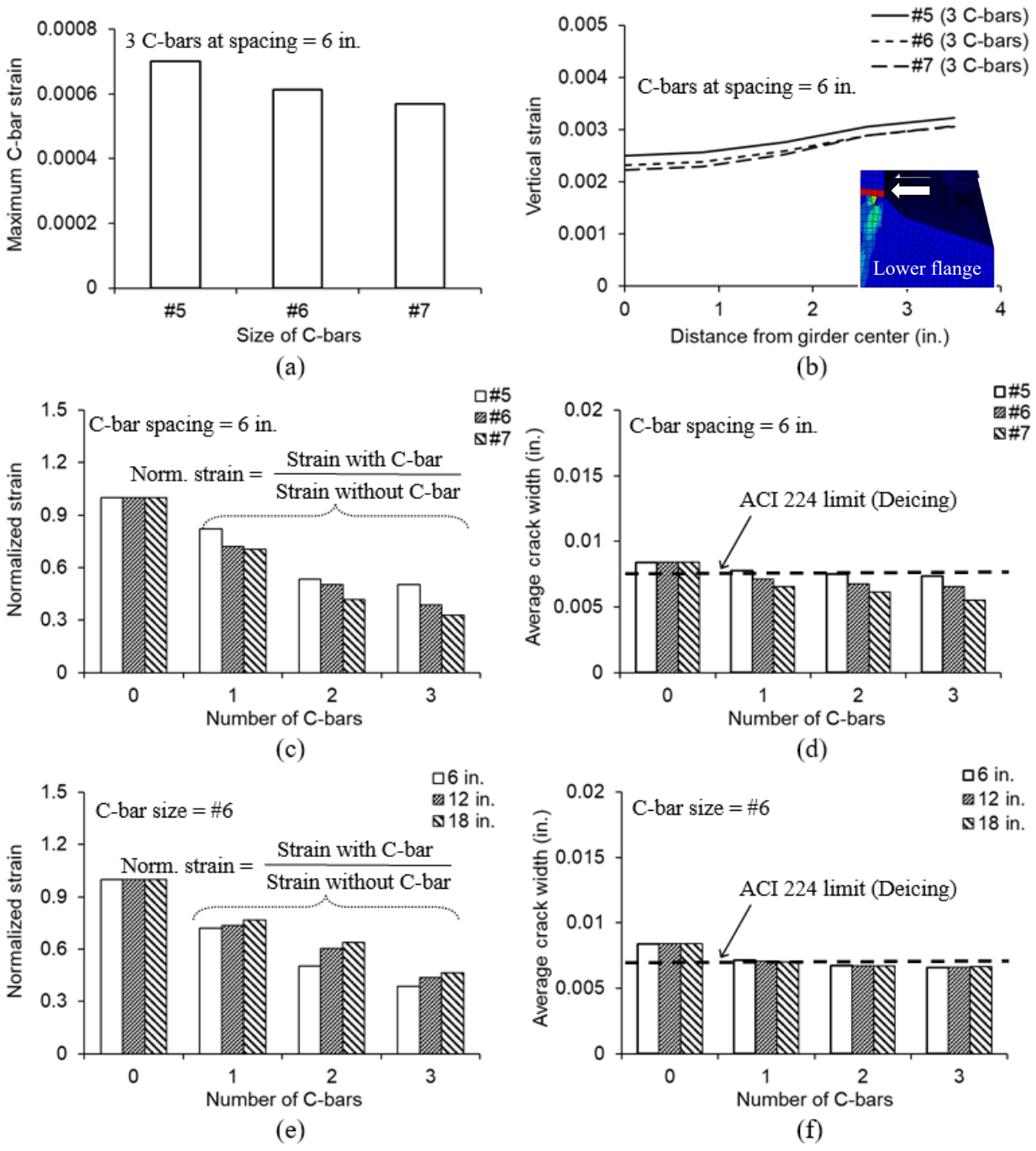

Fig. II.12. Variable C-bar configurations: (a) maximum strain with C-bar size; (b) vertical strain at junction between lower flange and web with C-bar size; (c) normalized vertical strain at 0.7*h* from girder bottom with C-bar size; (d) average long-term crack width with C-bar size; (e) normalized vertical strain at 0.7*h* from girder bottom with C-bar spacing; (f) average long-term crack width with C-bar spacing

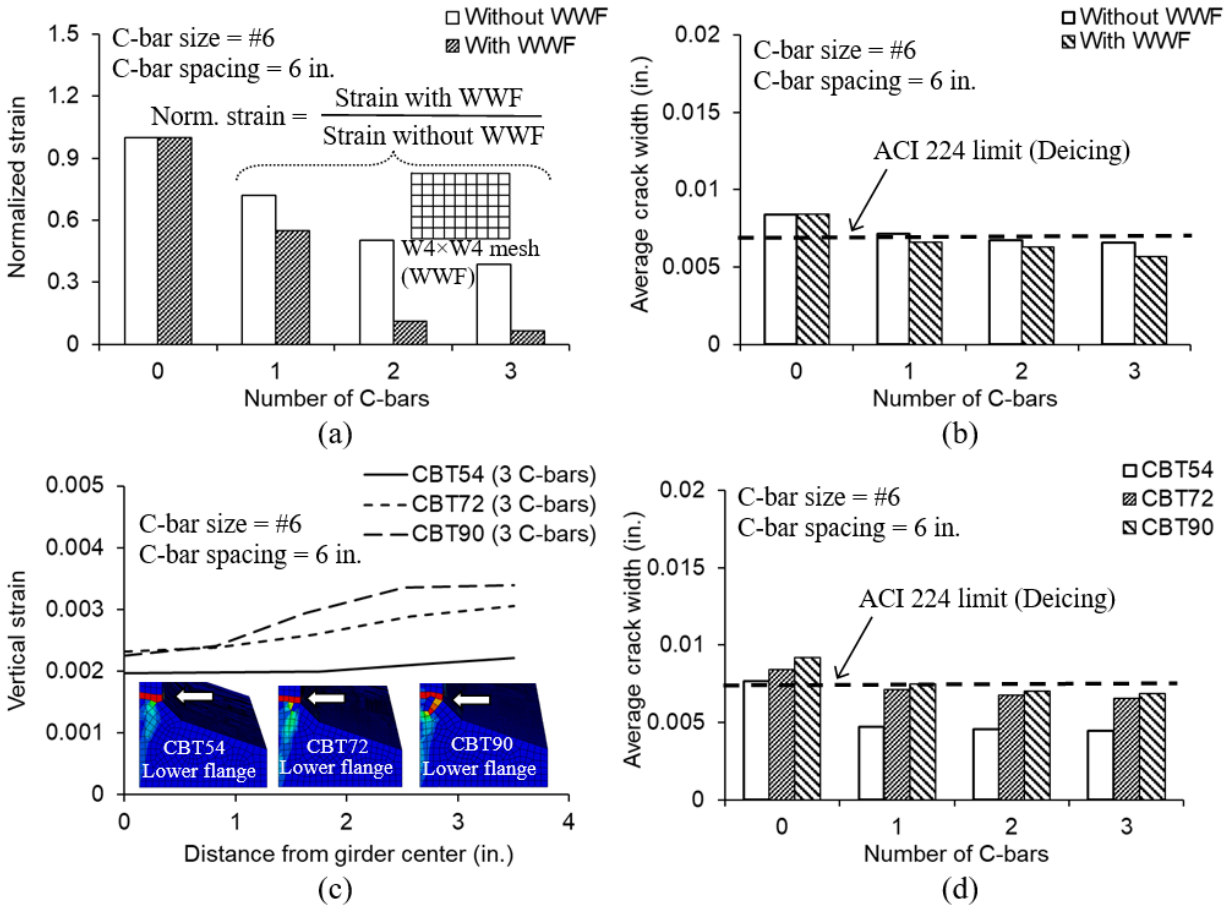

Fig. II.13. Welded wire fabric (WWF) and girder depth: (a) normalized vertical strain at 0.7*h* from girder bottom with and without WWF; (b) average long-term crack width with and without WWF; (c) vertical strain at junction between lower flange and web with girder depth; (d) average long-term crack with girder depth

II.6. Summary and Conclusions

This report has investigated the behavior of end zones in prestressed concrete bulb-tee girders with a variety of reinforcing schemes. The CBT72 girder from the Colorado Department of Transportation served as the default, utilizing C-bars and spirals intended to restrain cracks in the girder concrete. Three-dimensional finite element models were formulated to elucidate the consequences of modifying C-bar configurations. Of interest were the breadth of end zones, reinforcement responses, concrete strain fields, cracking patterns, damage amounts, and splitting forces. Parametric studies expanded the coverage of the simulations by taking into account assorted factors: C-bar properties (size and spacing), girder depth (CBT54 and CBT90), and welded wire fabric. Practical design aspects were highlighted. The following are concluded

- The growth of strand stress along the girder was not governed by the number of C-bars. The prestressing stress developed partially within the $h/4$ end zone set forth in the AASHTO LRFD Bridge Design Specifications (AASHTO 2020), while the empirical transfer length of $60d_b$ was deemed acceptable. The $3h/4$ limit was sufficient to envelop the maximum principal stresses in the girder web where the harped strands were placed.
- The maximum tensile strain of 652×10^{-6} in one C-bar just above the lower flange abated as the strain location shifted away from the girder bottom owing to a reduction in prestressing forces associated with the straight strands. The slanted strands in the web caused local compression of the C-bar. When multiple C-bars were positioned, stress redistributions brought about a decline in strain except for the first bar near the girder end. Spiral strains were insensitive to the quantity of the C-bars.
- The vertical strains of the girder concrete decreased by over 15.9% with the use of the C-bars, which was prominently manifested in the upper portion of the web, enabling relevant crack control. Even though the average short-term crack widths of the girder remained below the ACI limit of 0.007 in., the long-term widths were larger than the limit apart from the occasions with two and three C-bars.
- The inclined strands in the web were the notable source of splitting cracks coupled with the eccentricities of the strands. The refined and AASHTO equations resulted in equivalent splitting forces within the range of $0.2h$ to $0.7h$; outside this threshold, pronounced discrepancies were noticed on account of the terms dealing with the strands' eccentricities.
- The vertical concrete strains at the junction between the lower flange and web diminished as larger size C-bars were employed; by contrast, damage at that location went up with the girder depth. If there is no rebar congestion in the end zones, multiple No. 6 or No 7 C-bars spaced 6 in. apart together with welded wire fabric should be placed to minimize the growth of concrete strains and crack width.

II.7. References

AASHTO. 2020. AASHTO LRFD bridge design specifications (9th Edition), American Association of State Highway and Transportation Officials, Washington, D.C.

ABAQUS. 2016. Theory manual, Dassault Systemes, Velizy-Villacoublay, France.

Abdel-Jaber, H. and Glisic. B. 2019. Monitoring of prestressing forces in prestressed concrete structures- an overview, Structural Control and Health Monitoring, 26, e2374.

ACI. 2001. Control of cracking in concrete structures (ACI 224R-01), American Concrete Institute, Farmington Hills, MI.

ACI. 2008. Guide for modeling and calculating shrinkage and creep in hardened concrete (ACI 209.2R-08), American Concrete Institute, Farmington Hills, MI.

ACI. 2015. Guide to concrete floor and slab construction (ACI 302.1R-15), American Concrete Institute, Farmington Hills, MI.

Alfarah, B., Lopez-Almansa, F., and Oller, S. 2017. New methodology for calculating damage variables evolution in plastic damage model for RC structures, Engineering Structures, 132, 70-86.

Arab, A., Badie, S.S., Manzari, M.T., Khaleghi, B., Seguirant, S.J., and Chapman, D. 2014. Analytical investigation and monitoring of end-zone reinforcement of the Alaskan Way viaduct super girders, PCI Journal, 59(2), 109-128.

Boulbes, R.J. 2019. Troubleshooting finite-element modeling with Abaqus with application in structural engineering analysis, Springer, Berlin, Germany.

CDOT. 2022. CDOT bridge design manual, Colorado Department of Transportation, Denver, CO.

CEN. 2004. Eurocode 2: design of concrete structures (EN 1992-1-1:2004), European Committee for Standardization, Brussels, Belgium.

Ferreira, T., and Rashband, W. 2012. The ImageJ user guide, National Institute of Health, Bethesda, MD.

fib. 2009. Structural concrete: textbook on behaviour, design and performance, International Federation for Structural Concrete, Lausanne, Switzerland.

fib. 2010. Model Code 2010, Thomas Telford, London, UK.

Garg, A.K. and Abolmaali, A. 2009. Finite-element modeling and analysis of reinforced concrete box culverts, Journal of Transportation Engineering, 135(3), 121-128.

Guyon, Y. 1955. Prestressed concrete, Contractors Record, London, UK.

He, Z.-Q. and Liu, Z. 2011. Investigation of bursting forces in anchorage zones: compression-dispersion models and unified design equation, Journal of Bridge Engineering, 16(6), 820-827.

Hordijk, D.A. 1992. Tensile and tensile fatigue behavior of concrete: experiments, modeling and analyses. Heron, 37(1), 3-79.

Kratzig, W.B. and Polling, R. 2004. An elasto-plastic damage model for reinforced concrete with minimum number of material parameters, Computers and Structures, 82(15-16), 1201-1215.

Leonhardt, F. 1988. Cracks and crack control, PCI Journal, 33(4), 124-145.

Marshall, W.T. and Mattock, A.H. 1962. Control of horizontal cracking in the ends of pretensioned prestressed concrete girders, PCI Journal, 7(10), 56-75.

Mertz, D.R. 2008. AASHTO LRFD 2008 interim changes, Aspire, 2(1), 56.

Miura, T., Sato, K., and Nakamura, H. 2020. The role of microcracking on the compressive strength and stiffness of cracked concrete with different crack widths and angles evaluated by DIC, Cement and Concrete Composites, 114, 103768.

O'Callaghan, M.R. and Bayrak, O. 2008. Tensile stresses in the end zone regions of pretensioned I-beams at release, Technical Report: IAC-88-5DD1A003-1, Texas Department of Transportation, Austin, TX.

PCI. 2006. PCI manual for the evaluation and repair of precast, prestressed concrete bridge products, Precast/Prestressed Concrete Institute, Chicago, IL.

PCI. 2017. PCI design handbook (8th Edition), Precast/Prestressed Concrete Institute, Chicago, IL.

PCI. 2023. PCI bridge design manual (MNL-133-23), Precast/Prestressed Concrete Institute, Chicago, IL.

Ren, W., Sneed, L.H., Yang, Y., and He, R. 2015. Numerical simulation of prestressed precast concrete bridge deck panels using damage plasticity model, International Journal of Concrete Structures and Materials, 9(1), 45-54.

Ronanki, V.S., Burkhalter, D.I., Aaleti, S., Song, W., and Richardson, J.A. 2017. Experimental and analytical investigation of end zone cracking in BT-78 girders, Engineering Structures, 151, 503-517.

Ross, B.E., Willis, M.D., Hamilton, H.R., and Consolazio, G.R. 2014. Comparison of details for controlling end-region cracks in precast, pretensioned concrete I-girders, PCI Journal, 59(2), 96-108.

Salas, R.M., Schokker, A.J., West, J.S., Breen, J.E., and Kreger, M.E. 2008. Corrosion risk of bonded, post-tensioned concrete elements, PCI Journal, 53(1), 89-108.

Steinberg, E. and Semendary, L. 2017. Evaluation of revised details of end zone of the prestressed concrete I-girders using finite element method, Structure and Infrastructure Engineering, 13(11), 1390-1403.

Tadros, M.K., Badie, S.S., and Tuan. C.Y. 2010. Evaluation and repair procedures for precast/prestressed concrete girders with longitudinal cracking in the web, NCHRP Report 654, Transportation Research Board, Washington, D.C.

Ugural, A.C. and Fenster, S.K. 1995. Advanced strength and applied elasticity (3rd ed.), Prentice-Hall, Hoboken, NJ.

Wang, J., Basheer, P.A.M., Nanukuttan, S.V., Long, A.E., and Bai, Y. 2016. Influence of service loading and the resulting micro-cracks on chloride resistance of concrete, Construction and Building Materials, 108, 56-66.

Xiong, X., Zhang, Y., Ge, Y., Shi, H., Musa, M.M.E. and Yao, G. 2023. Shear behavior of full-scale prestressed concrete double tee beams with steel-wire meshes, Journal of Building Engineering, 64, 105464.

Yao, G., Xiong, X., and Ge, Y. 2021. Cracking behavior of full-scale pre-tensioned prestressed concrete double-tee members with steel-wire meshes, Journal of Building Engineering, 44, 102658.

Yapar, O., Basu, P.K., and Nordendale, N. 2015. Accurate finite element modeling of pretensioned prestressed concrete beams, Engineering Structures, 101, 163-178.